AN ABSTRACT OF THE THESIS OF

<u>Kavitha Srinivasan</u> for the degree of <u>Master of Science</u> in <u>Electrical and Computer Engineering</u> presented on <u>September 22, 2006.</u>

Title: <u>Computationally Efficient Substrate Noise Coupling Estimation in Lightly Doped Silicon Substrates.</u>

Abstract approved:

_____

Kartikeya Mayaram   Terri S. Fiez

A Z-parameter based macromodel for characterizing the substrate noise coupling in a lightly doped substrate at low frequencies has been developed. The model is scalable with contact geometries and separation. The cross-coupling impedance between two contacts is modeled using an improved geometric mean distance formulation. This approach obviates the need for using several spacing related parameters for describing the contact separations, sizes, and orientation. An improved self-impedance model has also been developed. Proximity effects of neighboring contacts are taken into account by a paneling approach. The macromodel with paneling has been successfully used to predict the noise coupling for multi-contact examples. The errors from the macromodel relative to a numerical simulator are within acceptable limits of 15%.

Computationally Efficient Substrate Noise Coupling Estimation in Lightly Doped Silicon

Substrates

by

Kavitha Srinivasan

A THESIS

submitted to

Oregon State University

in partial fulfillment of
the requirements for the
degree of

Master of Science

Presented September 22, 2006

Commencement June 2007

Master of Science thesis of Kavitha Srinivasan presented on September 22, 2006.

APPROVED:

_____

Co-Major Professor, representing Electrical and Computer Engineering

_____

Co-Major Professor, representing Electrical and Computer Engineering

_____

Director of the School of Electrical Engineering and Computer Science

_____

Dean of the Graduate School

I understand that my thesis will become part of the permanent collection of Oregon State University libraries. My signature below authorizes release of my thesis to any reader upon request.

_____

Kavitha Srinivasan, Author

ACKNOWLEDGEMENTS

To my Parents

TABLE OF CONTENTS

TABLE OF CONTENTS (Continued)

TABLE OF CONTENTS (Continued)

Page

LIST OF FIGURES

LIST OF APPENDIX FIGURES

LIST OF TABLES

LIST OF APPENDIX TABLES

Computationally Efficient Substrate Noise Coupling Estimation in Lightly Doped Silicon Substrates

1. INTRODUCTION

The digital revolution has driven the need for highly integrated analog, RF and digital systems to co-exist on a common silicon substrate. While this integration enhances speed and reduces power and cost, it brings with it the issue of substrate noise. A simplified representation of this issue is shown in Figure 1.1. The digital switching noise couples through the supply lines and the common substrate to the analog and RF blocks. This results in a performance degradation of the analog and RF blocks. The noise coupling increases with an increase in the frequency of operation and also with a decrease in the device dimensions, thus making substrate noise characterization crucial in the design cycle.
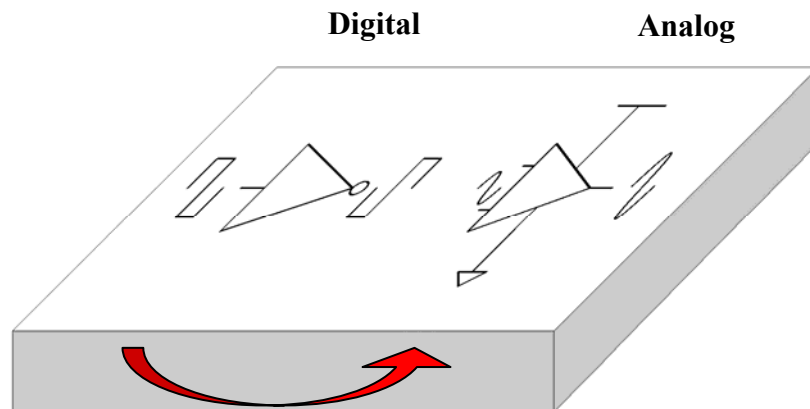
Digital   **Analog**

Figure 1.1. Substrate noise coupling from a digital circuit to an analog circuit.

The noise propagation properties of the substrate are strongly dependent on its doping levels. Based on the doping concentration, substrates can be classified into two primary types: lightly doped (high resistivity) substrates and heavily doped (low resistivity) substrates. Latchup issues in lightly doped substrates resulted in an increased popularity of epitaxial or heavily doped substrates. With technology scaling in recent years, the trend has shifted towards lower voltage operations, and hence latchup has become less of an issue [1]. In addition, an epitaxial substrate proves less effective in isolating the noisy digital blocks from the sensitive analog cells when the circuit is densely packed. In order to achieve better signal integrity, the lightly doped substrate is a preferred choice for today's ICs. This is true especially for applications where analog, RF and digital circuitry are integrated on the same die [2].

Since substrate noise is capable of degrading circuit performance, designers are looking for better ways to know *a-priori* the noise isolation that they can achieve and techniques to improve it. Pre-layout noise analysis at the schematic or cell level or during floor planning can be more beneficial than the traditional post-layout analysis. At the pre-layout level, a quick, yet reliable approximation of noise coupling between the noisy node and the sensitive node is required. Numerical methods to accurately characterize the substrate are readily available. Unfortunately, numerical methods are computationally expensive and thus time consuming. This makes them unsuitable for use during pre-layout. Accuracy can be traded-off for efficiency during the pre-layout noise estimation stage and hence there is a thrust to find quicker but less accurate solutions.

1.1. Summary of Previous Work and Contributions

As noted earlier, several accurate numerical methods characterize the lightly doped substrate. The methods can be classified into two broad categories: finite difference methods [3], [4] and boundary element methods [5], [6].

In finite difference methods (FDM) the entire volume of the substrate and the contacts placed on it are divided into a mesh and Poisson's equation is used to estimate the potential variation. The rigorous 3-D meshing makes it a time consuming method. In the boundary element method, the surfaces of the substrate contacts are divided into panels to solve equations for the potential variation. The method is faster than FDM, but is still not a good choice for noise estimation at the pre-layout stage.

Empirical models are alternatives to the numerical methods. They are obtained as a result of a curve fitting process applied to simulation or measured data [7], [8], [9]. Such, models often express noise coupling in terms of the geometry and the separation of the contacts. Unfortunately, empirical methods do not produce generalized models and, hence, cannot be applied to arbitrary substrates. In addition, several assumptions made while developing such models lead to accuracy issues when applied to situations where these assumptions are violated. However, the empirical models provide a quick estimation of noise coupling during the preliminary stages of circuit design.

This work focuses on developing a simple and reliable resistive macromodel that characterizes the lightly doped substrate up to frequencies of about a few gigahertz. A brief comparison with existing approaches and a summary of the contributions is:

- In [8], the effective coupling resistances are modeled directly. This can lead to issues when extending the two-port model to practical multi-contact situations. This work adopts a Z-parameter based approach to develop a general model.

- The model described in [9] has unacceptable errors when applied to very closely spaced contacts, i.e., of the order of 1~10μm. The model developed in this thesis provides better accuracy for these situations.

- In [7], a Z-parameter based model has been developed. The model requires several process constants and was validated for a few contact geometries and separations. The following work attempts to develop a compact model that works for a large set of contact geometries and separations.

1.2. Thesis Outline

The thesis is organized as follows: Chapter 2 discusses the properties of lightly doped substrates and the reasons for choosing open circuit parameters to model the resistive network. In Chapter 3, the model development for the cross-coupling impedance and the self-impedance is described. Chapter 4 explains a paneling approach and the application of the macromodel in conjunction with the paneling approach to account for the proximity effects of neighboring contacts. Chapter 5 provides comprehensive validation of the macromodel using measurements and simulations. The macromodel with paneling is applied to a multi-contact example to prove the usefulness of this work.

Finally Chapter 6 concludes the current work, and discusses the scope for future investigations.

2.   PROPERTIES OF THE LIGHTLY DOPED SUBSTRATE AND THE SUBSTRATE COUPLING NETWORK

In this chapter a discussion of the conductive properties of a non-uniform lightly doped substrate is provided. This is followed by a brief explanation for representing the lightly doped substrate with an equivalent network. Open-circuit parameters are used to characterize the substrate and hence the noise coupling. Measuring open-circuit parameters requires a reference. It is assumed that the backplane of the substrate can be chosen as the reference. The conditions under which this assumption is valid are discussed.

2.1. Conductive properties of lightly doped substrates

The lightly doped substrate is a high resistive substrate with bulk resistivities of the order of 10~50Ω-cm. Noise isolation can be improved by simply increasing the distance between the noisy and sensitive blocks [6]. However the high resistivity of such substrates is often decreased because of p$^+$ surface implants (for p-type substrates) such as channel-stop implants. Channel-stop implants are usually added to prevent the formation of parasitic paths [10]. A parasitic conductive layer may be formed when a high voltage is applied on a uniformly doped silicon surface (of p-type) without such implants. The conductivity of these implants is about two orders of magnitude more than the bulk. The implant depth is typically 1μm. The higher conductivity aids in increasing the threshold voltage of the surface and prevents a parasitic conduction path. However, the channel-stop implant makes the substrate more conductive at the surface and,

therefore, analog or RF circuits are not isolated to the fullest extent from the digital blocks.

To illustrate the above effect, the equivalent resistances for two contacts in a uniformly doped substrate and a substrate with a channel-stop implant are compared. The equivalent resistance is measured by injecting a unit current through one contact and measuring the potential on the other. The cross sections of the substrate profiles are shown in Figure 2.1. The resistances were extracted from a Green's function-based solver, EPIC [5]. An overview of the tool capabilities and assumptions are given in APPENDIX A. The plot of the equivalent coupling resistance between the two contacts as a function of separation is presented in Figure 2.2. The coupling resistance is an order of magnitude lower in the substrate with channel-stop implants. All the substrates reported in this work are assumed to have a channel-stop implant.

(a)   (b)
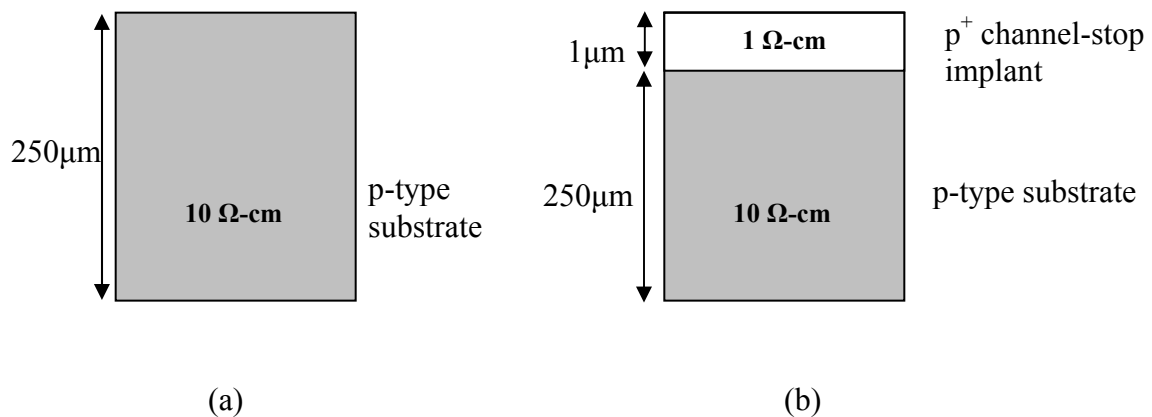
Figure 2.1. Cross sections of lightly doped substrates. (a) Uniform lightly doped substrate. (b) Lightly doped substrate with channel-stop implant.
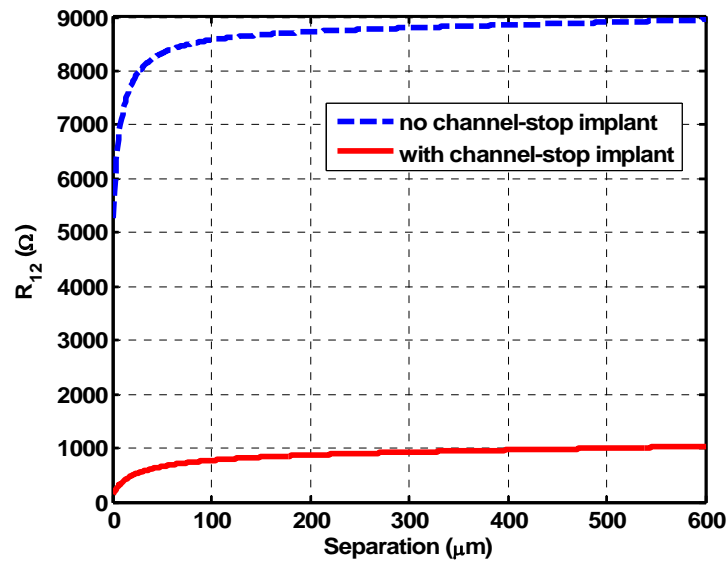
Figure 2.2. Comparison of the equivalent coupling resistances for a lightly doped substrate with and without a channel-stop implant.

2.2. Equivalent substrate network for lightly doped substrates

For frequencies less than a few gigahertz, the coupling between two contacts in a substrate can be represented equivalently by a resistive π-model as shown in Figure 2.3 [7], [8], [9]. R_{12} represents the cross-coupling resistance and R_{11} or R_{22} characterize the mutual resistance between the contact and the backplane.
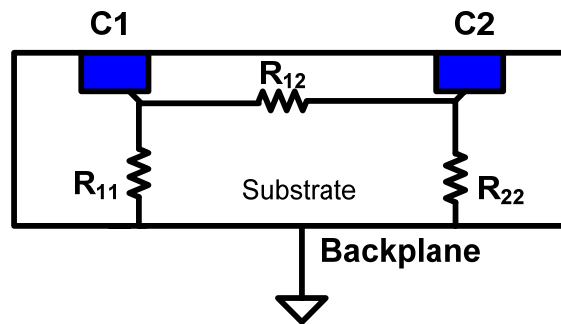
Figure 2.3. A π-resistive model.

The open circuit or Z-parameters are used to characterize the substrate network. To illustrate the open circuit parameters, consider in general a set of contacts on the substrate. If **V** is the vector of voltages applied on contacts, **I** is the vector of currents that is conducted by the substrate and **Z** is the impedance matrix, then the current-voltage relationship is given by

$$[\mathbf{V}] = [\mathbf{Z}]*[\mathbf{I}] \tag{2.1}$$

For a simple case of two contacts, the above relation can be written as:

$$\begin{bmatrix} V_1 \\ V_2 \end{bmatrix} = \begin{bmatrix} Z_{11} & Z_{12} \\ Z_{21} & Z_{22} \end{bmatrix} \begin{bmatrix} I_1 \\ I_2 \end{bmatrix} \tag{2.2}$$

where Z_{ii} is the self-impedance, or the potential at contact Ci when a unit current is injected into it while the other contact Cj (j≠i) is kept floating. Z_{ij} (i≠j) is the cross-coupling impedance, or the potential on a floating contact Ci, when a unit current is injected into the other contact Cj. The impedances are given by the following expressions:

$$Z_{ii} = \left(\frac{V_i}{I_i} \right)_{I_j = 0} \qquad\qquad Z_{ij} = \left(\frac{V_i}{I_j} \right)_{I_i = 0} \tag{2.3}$$

By the principle of reciprocity, $Z_{ij} = Z_{ji}$. The Z-parameters are a function of the sizes and separation of the two contacts for a given substrate. This fact is used to model these parameters in this work. The Z-parameters can be related to the resistive network shown in Figure 2.3 by the following relations:

$$Z_{ii} = R_{ii} \parallel (R_{ij} + R_{jj}) \qquad\qquad Z_{ij} = \frac{R_{ii} R_{jj}}{R_{ii} + R_{jj} + R_{ij}} \tag{2.4}$$

Open circuit parameters are chosen to model the substrate because they are largely independent of the surrounding contacts. This follows from the fact that the surrounding contacts are open circuited or left floating while measuring the self-impedance for a contact (C1 or C2) and the cross-coupling impedance between the two contacts (C1 and C2). The two-contact problem can be easily extended to multi-contacts by individually computing the Z matrix for every pair of contacts. This property is not exhibited by the resistance matrix or the admittance matrix, which makes them unsuitable to characterize the substrate network [11]. Finally, to extract the resistance network for a multi-contact case, the **Z**-matrix can be inverted to obtain the admittance matrix and the resistances can be calculated from this admittance matrix (Section 4.2).

Characterization of a lightly doped substrate is a more involved problem compared to characterizing a heavily doped substrate. After a certain threshold separation, a heavily doped substrate conducts mainly through its bulk and not through the surface. Beyond this threshold separation, the cross-coupling resistance between any two contacts becomes too large and the cross-coupling impedance becomes negligible (from Equation (2.4)). Hence, there is a specific range of separations for which characterization is required. Due to the presence of a channel-stop implant, conduction takes place through the surface in a lightly doped substrate even for large separations. This indicates that the coupling resistance is not large enough at far separations and, hence, the cross-coupling impedance cannot be neglected [6].

2.3. Backplane properties of a lightly doped substrate

Open circuit parameters require a reference for their measurements. For a substrate network, the backplane is often chosen to be the reference. Consequently the backplane would have to be assumed equipotential. The backplane is usually not considered equipotential for a lightly doped substrate [12]. However, the backplane can be approximated as an equipotential surface for certain conditions as explained in this section.

If the backplane of a substrate is floating the equivalent network for a two-contact case consists simply of an *effective cross-coupling resistance* (R_{12f}). This cross-coupling resistance (R_{12f}) can be extracted from the grounded backplane network provided the backplane is an equipotential surface (Equation (2.5)) as shown by Figure 2.4.

$$R_{12f} = R_{12} \parallel (R_{11} + R_{22}) \tag{2.5}$$
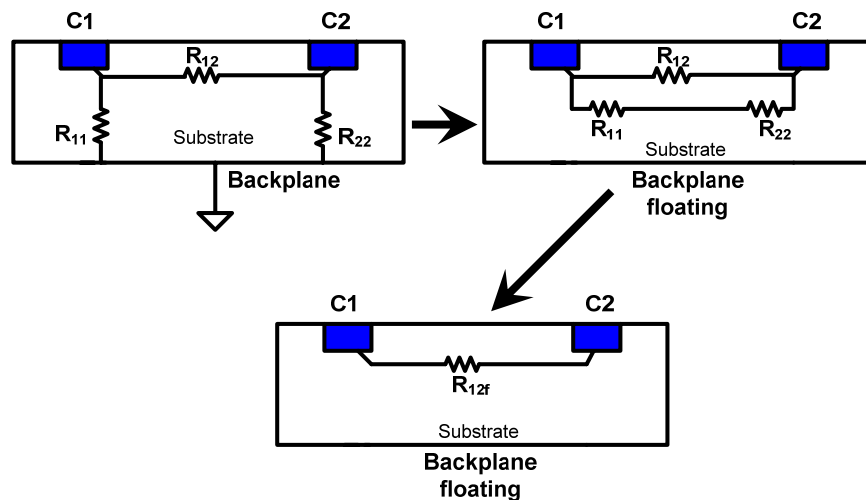
Figure 2.4. Floating backplane substrate network derived from a π-resistive network.

If the relation in Equation (2.5) for two contacts is valid for the lightly doped substrate under consideration (Figure 2.2(b)) then the backplane can be approximated as a single node. First the above equation is validated for two-contact cases. Then multi contact examples are considered. For the latter case, SPICE is used to obtain the effective floating cross-coupling resistances from the grounded backplane network and compared with the actual floating backplane substrate resistances. All the above validations were conducted using EPIC simulations using an option for grounding or floating the substrate backplane.

The results obtained for one of the two-contact cases is shown in Figure 2.5.
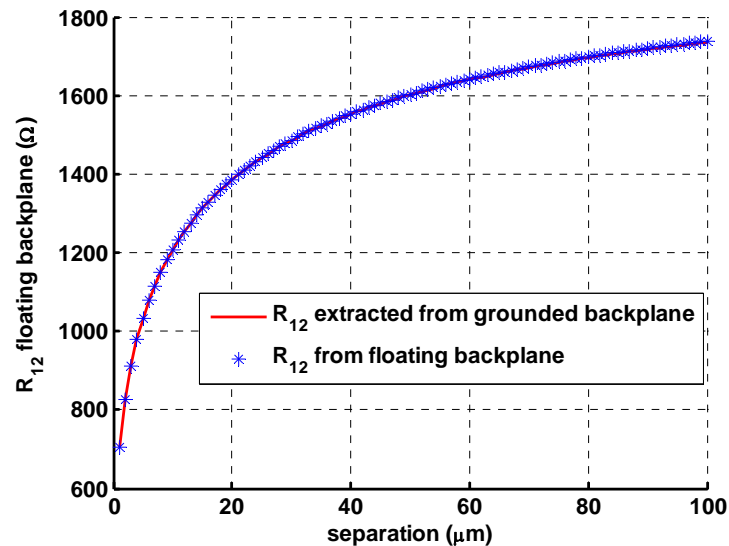
Figure 2.5. Comparison of the *effective cross-coupling resistances* between two contacts from a floating backplane setup and those derived from a grounded backplane.

The comparison between the backplane floating substrate resistances, and the resistances derived from the backplane grounded substrates for the multi-contact case is made in Table 2.1. The contact layout for this example is given in Figure 2.6. In both the

experiments the relative errors for all cases are less than 1% when the effective coupling resistances are compared.
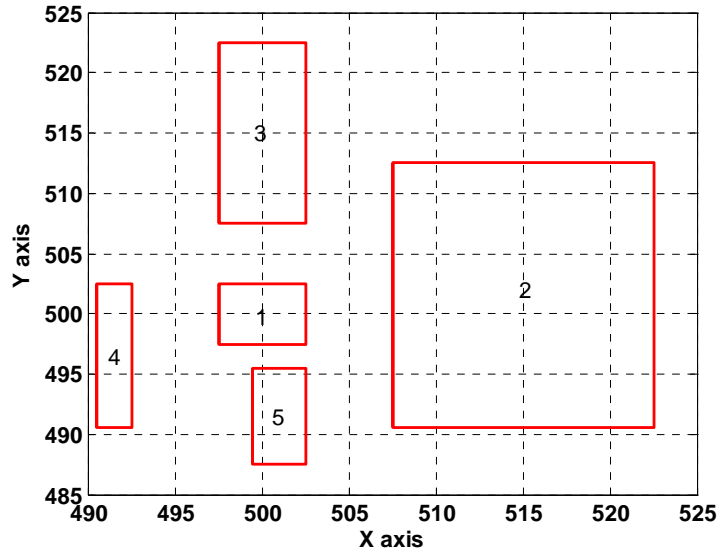
Figure 2.6. Layout of 5 non-identical contacts with dimensions (1) 5µm × 5µm, (2)15µm × 22.5µm, (3) 5µm × 15µm, and (4) 2.5µm × 12µm, and (5) 3µm × 8µm.

Table 2.1. Comparison of the *effective cross-coupling resistances* from a floating backplane setup and those derived from a grounded backplane for a multi-contact case.

R_{ij}	From floating backplane (Ω)	Extracted from grounded backplane (Ω)
R_{12}	277.6	277.56
R_{23}	369.56	369.42
R_{34}	397.03	396.96
R_{45}	398.05	397.99

Another example of a multi-contact case with large contacts placed at various locations of a 1mm × 1mm die is presented in Table B-1 of Appendix B. The maximum relative errors are about 16%. This serves as yet another proof for the claim that the backplane of this substrate can be considered equipotential with a reasonable accuracy. In addition, the same multi-contact example is considered to validate the equipotential backplane assumption for a resistive ground connection and is also presented in Appendix B, following the previous experiment. From the analyses of two-contact and multi-contact examples, it can be concluded that the backplane of this lightly doped substrate can be approximated as an equipotential surface with a reasonable accuracy.

The substrate thickness plays an important role in the equipotential approximation. In order to analyze the backplane characteristics for lightly doped substrates, tests were conducted with varying bulk thicknesses from 10μm to 250μm using the MEDICI device simulator [13]. A die width of 240μm was assumed, as only a limited number of grid points could be used in MEDICI. Three contacts were considered on the substrate's surface. A potential of 1V was applied on one contact placed in the middle of the die while grounding the other two contacts (Figure 2.7). The potential variation from one edge of the backplane to the other was measured for all substrates.
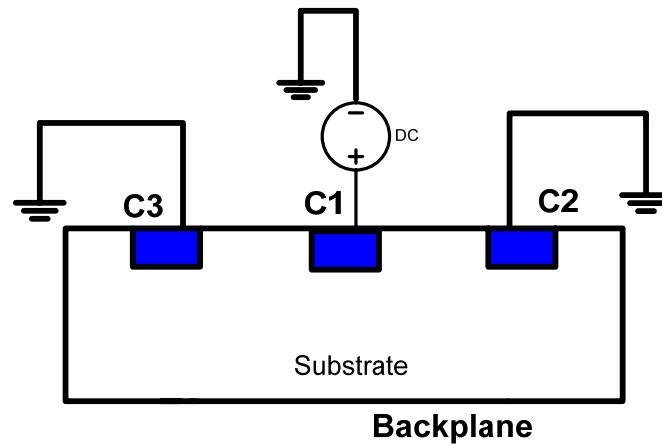
Figure 2.7. Simulation setup for measuring the backplane potential variation.

Assume that for any applied voltage x, Δx is the potential variation across the backplane. It was observed that there was a linear relationship between the voltage applied and the voltage at the backplane ($\Delta x = kx$). Hence the reference for measuring the potential variation across the backplane was taken to be the applied voltage. The backplane potential variation relative to the applied voltage for different substrate thicknesses is summarized in Table 2.2. The potential variation across the backplane plots is shown for a 250μm thick substrate in Figure 2.8 and for a 10μm thick substrate in Figure 2.9. The potential variation for a 10μm thick substrate is around 90% whereas it is approximately 10% for the 250μm thick substrate, with respect to the applied voltage. From the above observations it is clear that the potential across the backplane varies by significant amounts only for substrates with thicknesses less than 200μm.

Table 2.2. Potential variation across the backplane for different substrate
thicknesses relative to the applied voltage.

Substrate thickness (µm)	Relative backplane potential variation
10	90%
100	50~60%
200	18~20%
250	1~10%

The reason behind such a variation can be explained as follows. For thicker
substrates an electric charge placed on the substrate's surface views the entire backplane
as a point object and hence the variation in potential across the whole backplane is
minimized. After observing the potential variation for the various substrate thicknesses it
was concluded that the assumption of an equipotential backplane is valid for substrates
with thicknesses greater than 200µm. To further demonstrate that the backplane of
thinner substrates cannot be considered equipotential, a 100µm thick substrate with five
large contacts placed on it is considered in Appendix B. The effective floating cross-
coupling resistances derived from a grounded backplane and the actual floating
backplane resistances are compared in Table B-2. EPIC was used for simulating the
networks. The maximum relative errors are of the order of 40% when this backplane was
considered as an equipotential surface.
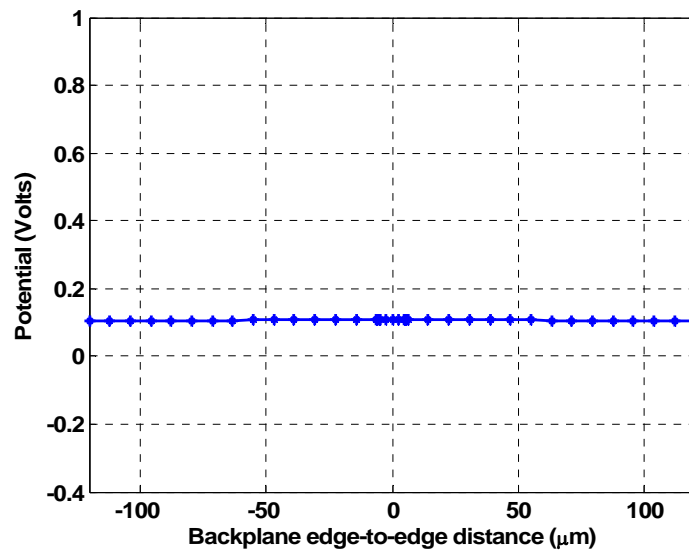
Figure 2.8. Potential variation across the backplane for a 250µm thick substrate.
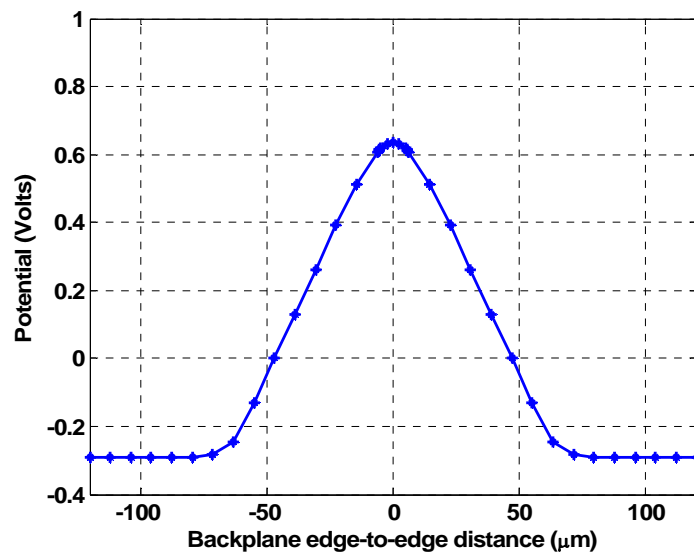
Figure 2.9. Potential variation across the backplane for a 10µm thick substrate.

3. MACROMODEL FOR LIGHTLY DOPED SILICON SUBSTRATES

In Chapter 2, a brief overview of the conductive properties of a lightly doped substrate was provided. The assumption that the backplane of the substrate can be considered to be an equipotential surface was validated. It was also noted that the Z-parameters of the substrate depend on the geometry and separation of the contacts. Given this background, the goal of this work is to develop a model that expresses the Z-parameters as a function of geometry and separation of the contacts.

This chapter focuses on the development of a model for the Z-parameters of a lightly doped substrate. The model is initially developed for a simple case of two contacts for a typical $0.25\mu m$ process. EPIC is used to simulate the Z-parameters for several contact cases and provides the basis for model development and validation.

3.1. Existing models

There are two main parametric approaches to model the noise coupling for lightly doped substrates. These approaches differ in the manner in which the geometry and separation of contacts are quantified.

In [7], the relative position of contacts is described separately along the *X* and *Y* axes. A drawback of this approach is that several process constants are needed to model the Z-parameters. In addition, effects such as proximity of neighboring contacts are not accounted when applying the model to multiple contacts. As a result, this model may not be adequate for large examples.

The model developed in [9] employs the geometric mean distance (GMD) to measure the contact separation. The GMD based approach eliminates the use of separate parameters to define the contact positions along the *X* and *Y* axes. The model is very efficient, especially for arbitrarily placed contacts. A single parameter (GMD) describes the relative positions of the contacts and as a result the number of process parameters is minimized. However, the geometric mean distance suffers from certain limitations leading to a significant loss of accuracy in practical situations, as will be discussed in Section 3.3.

3.2. Assumptions for the macromodel development

In Chapter 2, preliminary simulations showed that the effective circuit parameters for a floating backplane substrate can be derived from the Z-parameters of a grounded backplane substrate. It was also validated that the backplane of substrates with thicknesses > 200μm can be considered equipotential. A typical high resistive substrate closely depicting a 0.25μm process is shown in Figure 3.1. Assuming that the substrate is grounded, EPIC was used to extract the Z-parameters for a large set of two contact geometries (115 test cases listed in Table C-1 of Appendix C). The contact dimensions in the test cases range from 1μm to 200μm. A large variation in the data set was chosen to ensure that the model will work for a large set of geometries. The die size is assumed to be 1mm×1mm. The test cases consider different contact geometries that include squares and rectangles placed in different orientations. The types of contacts and orientations considered are described in Appendix C.

| 1μm | 0.1 Ω-cm | p^+ channel-stop implant |
| 250μm | 10 Ω-cm | p-type substrate |
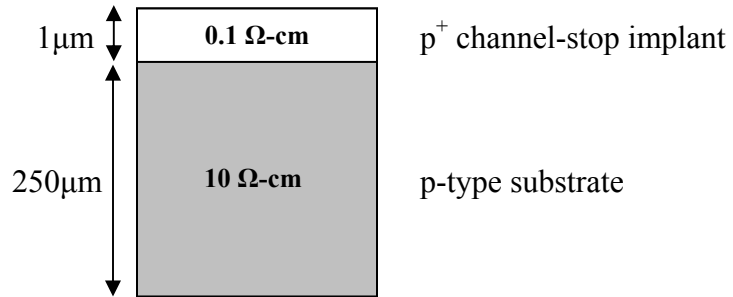
Figure 3.1. Cross section of a lightly doped substrate for a typical 0.25μm process.

The coupling trends between two contacts in the substrate are analyzed by systematically placing the contacts in several locations on the die by either increasing their edge-to-edge or center-to-center separations. The definitions of these separations between a pair of contacts are shown in Figure 3.2.

edge-to-edge separation

center-to-center separation

(a)

(b)
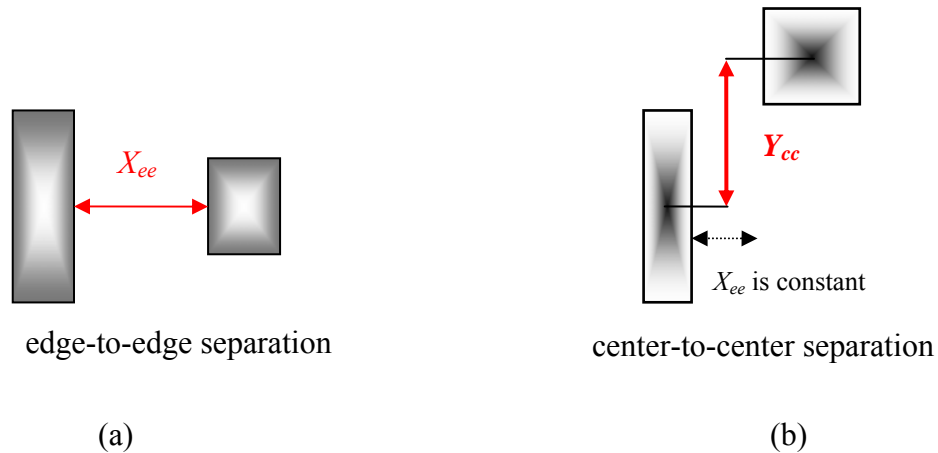
Figure 3.2. Convention of X_{ee} and Y_{cc} separation between contacts. (a) Edge-to-edge separation or X_{ee} separation. (b) Center-to-center separation or Y_{cc} separation.

The distance X_{ee} denotes the horizontal separation between the closest edges of the contacts, i.e., the edge-to-edge separation. The distance Y_{cc} represents the vertical separation between the centers of the contacts, i.e., center-to-center separation.

3.3. Geometric Mean Distance (GMD)

The geometric mean distance (GMD) was introduced in [8] to measure the effective separation between contacts. In [8], the GMD was used to model the cross-coupling resistance between the contacts. A similar approach to model the cross-coupling impedance or Z_{12} is followed in this thesis. One significant advantage of the GMD is that it simultaneously incorporates the effects of separation between contacts, their sizes and orientation. The GMD eliminates the need to individually consider the effect of these parameters.

The definition of geometric mean distance between two contacts is given by:

$$\ln d_{GMD} = \frac{\int_{L_2} \int_{W_2} \int_{L_1} \int_{W_1} \ln r \, dw_1 dl_1 dw_2 dl_2}{W_1 L_1 W_2 L_2} \tag{3.1}$$

where d_{GMD} is the geometric mean distance and r is the Euclidean distance between arbitrary points (w_1, l_1) and (w_2, l_2) on the contacts C1 and C2, respectively as shown in Figure 3.3 [14]. W_1, L_1, W_2, L_2 are the widths and lengths of contacts C1 and C2, respectively. The actual expression can be simplified [8], and is of the form:

$$gmd \cong (d_1 d_2 ..... d_{16})^{\frac{1}{16}} \tag{3.2}$$

where d_i is the Euclidean distance between the midpoints of the edges of the contacts (8 midpoints yielding 16 distances).
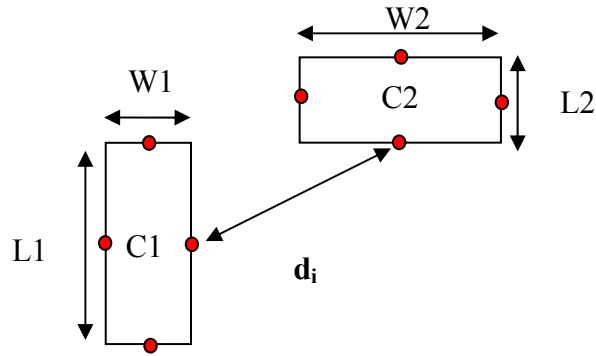
Figure 3.3. Geometric mean distance between two contacts using midpoints.

3.3.1. Limitations of the GMD

Experiments similar to the ones performed in [15] have been conducted for a given pair of contacts in a lightly doped substrate. First the Z_{12} dependence on GMD is checked to see if it is a unique function of the GMD. Then conditions under which Z_{12} is a unique function of the GMD are determined.

In order to determine how Z_{12} is influenced by the GMD, the first set of simulations consists of two experiments:

- Experiment 1: Analyze the relationship between Z_{12} and GMD for a two contact case by varying X_{ee}, keeping $Y_{cc}=0$. In other words, the centers of the contacts are aligned (Figure 3.2(a)).

- Experiment 2: Analyze the relationship between Z_{12} and GMD for a two contact case by varying Y_{cc} between the contacts and keeping X_{ee} fixed at 2μm (Figure 3.2(b)).

The results from these experiments are shown in Figure 3.4. Assume that the cross-coupling impedance is a function of the GMD alone. Then similar GMD values

from these experiments must generate identical Z_{12} values. According to Figure 3.4, at large values of GMD Z_{12} values obtained from both the experiments coincide. However, at closer separations (indicated by small values of GMD), Z_{12} values from both experiments do not match.
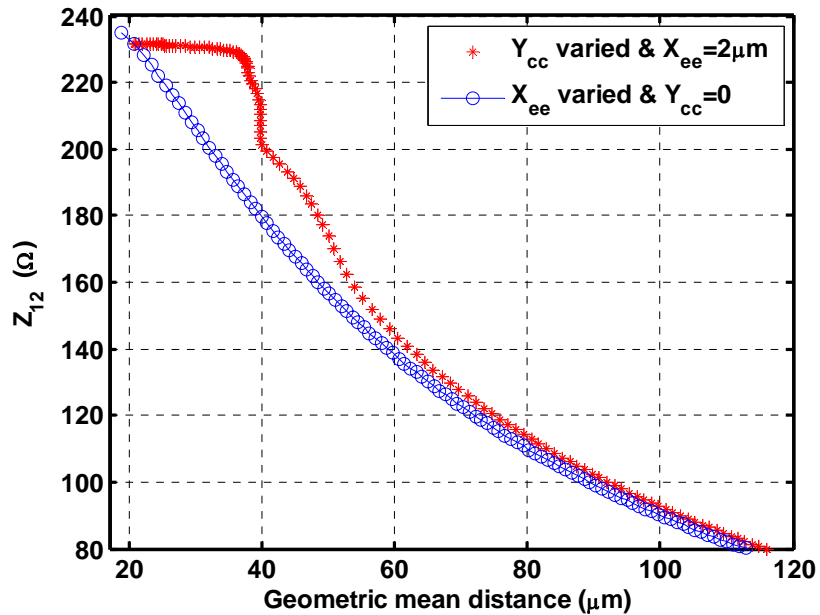
Figure 3.4. Plot of Z_{12} values from EPIC, as a function of GMD for 2 contacts (1µm × 110µm and 5µm × 27µm).

Figure 3.5 shows one such instance where identical GMD values do not result in similar Z_{12} values. The GMD is identical in both cases, but the Z_{12} is lower by 17% in the first case (Experiment 1) compared to the second case (Experiment 2). A possible explanation for this discrepancy is as follows: in Case 2, the contacts tend to remain in proximity, even though Y_{cc} is changed. However, this is not the situation in Case 1. The proximity effects influence Z_{12}, in addition to the GMD. As a result, Z_{12} tends to be higher. Hence,

for contacts placed at very close separations, GMD alone cannot model the behavior of Z_{12}.
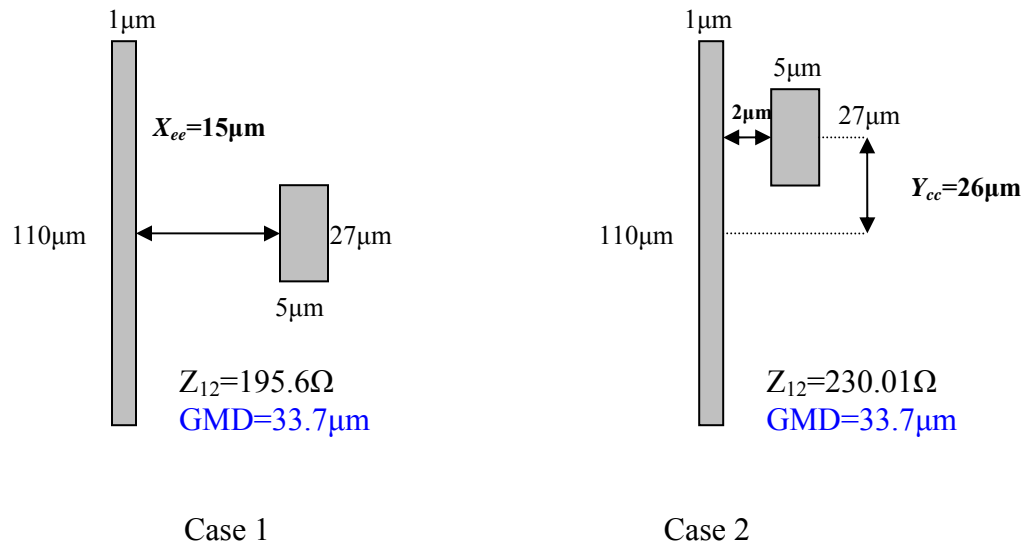
Figure 3.5. Example to show identical GMD representing different cross-coupling impedance values.

In the above analysis, it is seen that there exist certain cases when Z_{12} is not dependent on the GMD alone. Therefore, specific regions where Z_{12} is not dependent solely on GMD need to be identified, for a given process.

In Experiment 2, the X_{ee} separation is varied at regular intervals, say, 2μm, 10μm, 20μm, 50μm. For each X_{ee} separation, the Y_{cc} distance is varied and the cross-coupling impedances are extracted from EPIC. A plot of Z_{12} as a function of GMD is obtained for each X_{ee} separation and is shown in Figure 3.6. The Z_{12} vs. GMD obtained from Experiment 1 is plotted on the same figure. If the GMD uniquely defines Z_{12} at all X_{ee} and Y_{cc} separations, then all the plots would coincide. However, this is not the case and the

relative errors for Z_{12} (compared to the Z_{12} values from X_{ee} separation with Y_{cc}=0) reduce from 17% to close to 0% as X_{ee} increases. It is seen that Z_{12} is a unique function of the GMD for separations where $X_{ee} > 20\mu m$, for the given substrate and contacts.
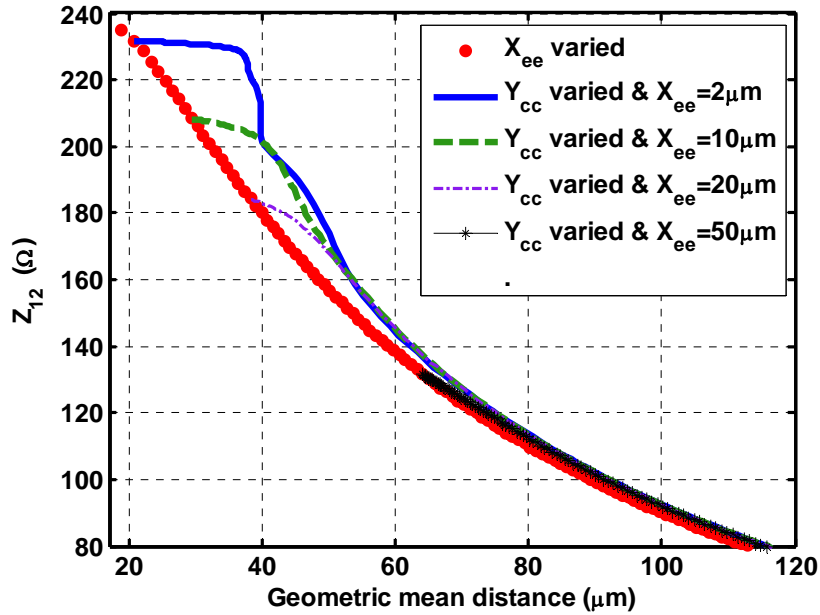
Figure 3.6. Z_{12} as a function of GMD for different X_{ee} separations when Y_{cc} is varied.

When the above experiments were repeated for contacts with different geometries, it was observed that the errors were more pronounced as the length of the contacts increased for relatively small X_{ee}. Clearly, the geometric mean distance is not adequate for correctly modeling the cross-coupling impedances at very close separations. The GMD should be used with a correction parameter to model all regions accurately.

3.4. Cross-coupling impedance (Z_{12}) model

With the understanding gained from the previous section, the modeling of Z_{12} for a simple case of two contacts is discussed. The model development is decomposed into three steps. They are as follows:

i. Assume $Y_{cc} = 0$, vary X_{ee}, and model Z_{12} as a function of GMD. In other words, model the impedances when contact centers are aligned.

ii. Next, assume $Y_{cc} \neq 0$ and use the above GMD model to characterize the cross-coupling impedance. In other words, model the Z_{12} when contact centers are mis-aligned

iii. Use a correction parameter to model the regions where GMD does not characterize the cross-coupling impedance between contacts correctly.

3.4.1. Z_{12} model for contacts with centers aligned

The Z_{12} is extracted by placing the contacts in the center of the die and X_{ee} is varied from 1μm to 600μm keeping Y_{cc}=0 (Figure 3.2(a)). The range 1μm to 600μm is chosen since the largest contacts in the set are squares with a dimension of 200μm. The squares can be separated by a maximum of 600μm in a 1mm×1mm die.

Using the extracted EPIC results, an exponentially decreasing function of the geometric mean distance is used to model the mutual coupling. An expression for Z_{12} (centers aligned) that follows the EPIC trend is as follows:

$$Z_{12(C-C)} = a_1 e^{-k_3 \sqrt{gmd}}$$

(3.3)

where a_1 is a function of the geometry of the two contacts and $k_3=0.19(\mu m)^{-(0.5)}$ is a process constant. The curve fitting procedure is outlined in APPENDIX D. The relative errors between the EPIC simulations and model results were found to be within ±10% for a large set of geometries and separation. The comparison between EPIC simulations and the GMD model equation for four different cases is shown in Figure 3.7.
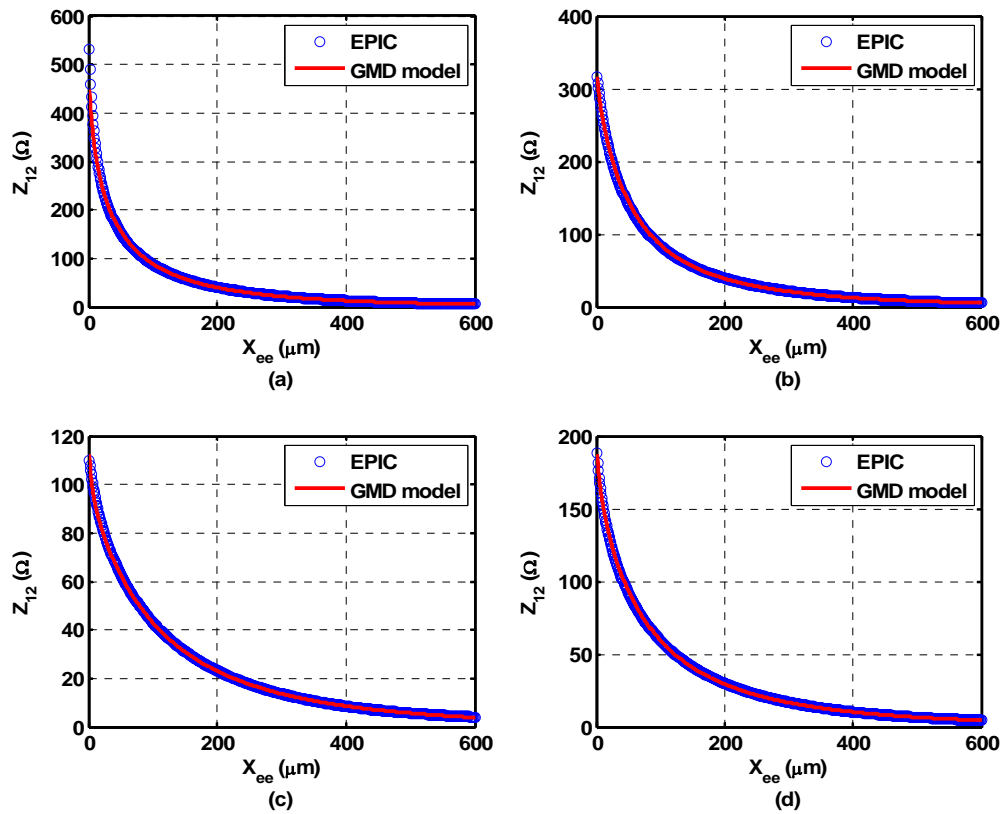
Figure 3.7. Comparison of the GMD model for Z_{12} and EPIC simulation results. The contact dimensions are (a) 3μm × 2.4μm and 2μm × 1μm, (b) 5μm × 40μm and 5μm × 40μm, (c) 100μm × 100μm and 100μm × 100μm, and (d) 60μm × 2μm and 45μm × 1μm.

Next, the parameter a_1 has to be modeled as a function of geometry. The parameter a_1 cannot be modeled as the merged self-impedance as suggested in [9] based

on the trends observed for different contact geometries (Figure 3.8(a)). The parameter a_1 is modeled as a linear function of the sum of widths of the two contacts as given below.

$$a_1 = k_1(sum\_of\_widths) + k_2 \qquad (3.4)$$

where k_1 and k_2 are process constants and *sum_of_widths* is the sum of w_1 and w_2 (Figure 3.3). This equation fits the a_1 values extracted from the model with a relative error of $\pm 6\%$ as shown in Figure 3.8(b).
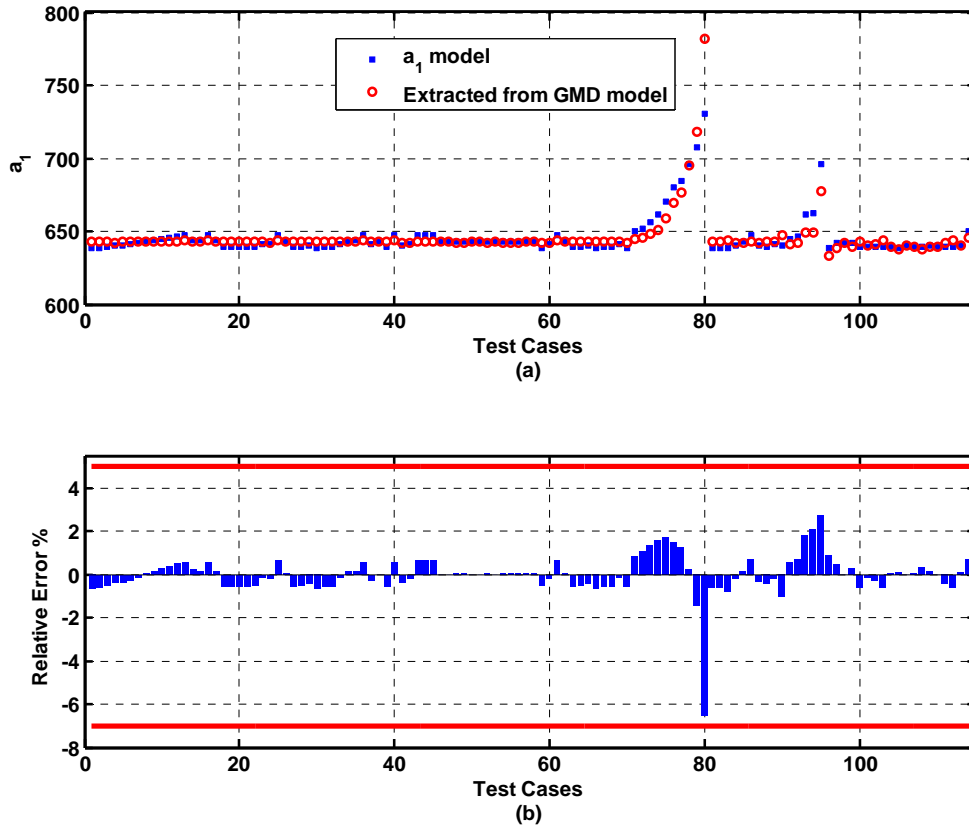
Figure 3.8. a_1 as a function of geometry. (a) Comparison of the a_1 model with extracted values from the GMD model. (b) Relative errors for the a_1 model compared to the extracted values from the GMD model.

Since the GMD encapsulates the dependence of the cross-coupling impedance on the size and orientation of contacts, a_1 is a simpler function. Given this a_1 model, the cross-coupling impedance of two contacts when their centers are aligned ($Z_{12(c-c)}$) can be represented by the following equation.

$$Z_{12(C-C)} = [k_1(w_1 + w_2) + k_2]e^{-k_3\sqrt{gmd}} \tag{3.5}$$

where k_1, k_2 and k_3 are process constants and w_1 and w_2 are the widths of the two contacts (Figure 3.3). To summarize, the parameters of this model are extracted by a two-step curve fitting approach:

1. In the first step, Z_{12} is modeled as a function of GMD. Values of a_1 are obtained for different geometries from curve fitting. k_3 is extracted as a process constant.

2. In the second step, a_1 is modeled as a function of the contact geometries. k_1 and k_2 are extracted as process constants, from the curve fitting process.

Equation (3.5) can be directly used to fit the Z_{12} simulation data instead of the two-step curve fitting and reduce the errors. From such a direct curve fitting approach the values of the process constants are:

$$k_1 = 0.2322\ \Omega\ (\mu m)^{-1} \qquad k_2 = 638\ \Omega \qquad k_3 = 0.195\ (\mu m)^{-0.5}$$

The relative errors between the model and EPIC simulations are within ±10% for a large range of geometries and separations. The relative errors increase more than 10% for very small contacts (which are below a dimension of 5µm) at separations less than 5µm. The model is also limited to contact geometries with length ratios (L_1/L_2 or L_2/L_1) less than 100. The comparison of the model equation with EPIC values for another four cases is shown in Figure 3.9, where the entire model (Equation (3.5)) has been employed.
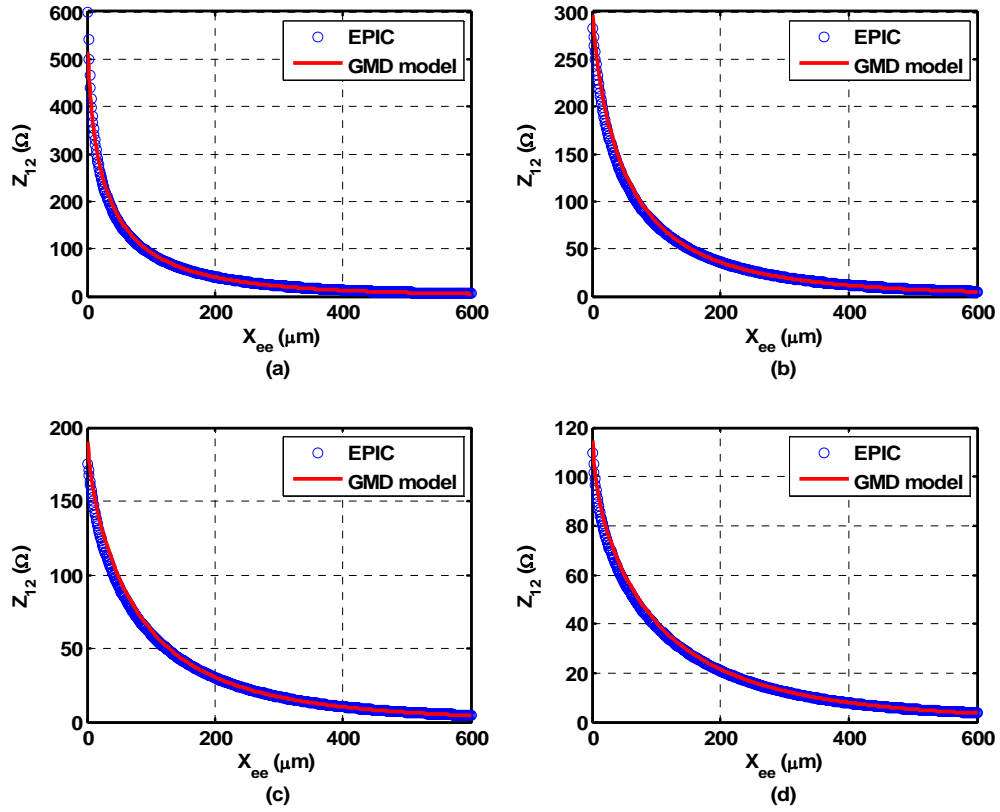
Figure 3.9. Comparison of the GMD model (Equation (3.5)) with EPIC simulations. The contact dimensions are (a) 1.2μm×1.2μm and 1.2μm×1.2μm, (b) 25μm×7μm and 16μm×20μm, (c) 50μm×50μm and 50μm×50μm, and (d) 125μm×1μm and 125μm×1μm.

A compact equation with just 3 process constants has been developed to model the cross-coupling impedance between contacts that have aligned centers. The next step is to model the cross-coupling impedance for contacts where the centers are not aligned.

3.4.2. Z_{12} model for contacts with centers not aligned

In practical layouts, the contacts or ports are placed arbitrarily, often with their centers not aligned. The model developed in the previous section is reasonably accurate

when the centers are aligned. The subsequent step is to evaluate the performance of the model equation (Equation (3.5)) by applying it to contact cases where the centers are misaligned. Impedances were extracted from EPIC using the same geometric data set, but with Y_{cc} varied from 0µm to 400µm and X_{ee} held constant (Figure 3.2(b)). The process is repeated for different X_{ee} (4µm, 6µm, 10µm and 50µm) to cover contact cases from near field to far field.
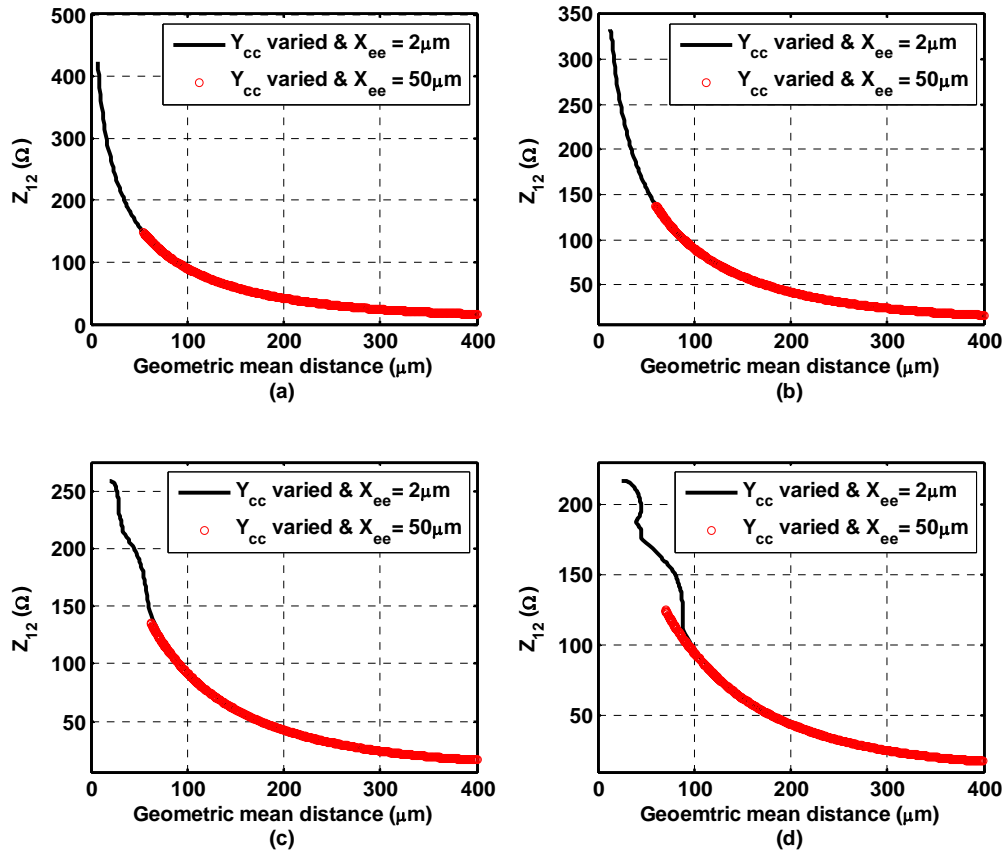
Figure 3.10. Behavior of mutual coupling with Y_{cc} separation. The contact dimensions are (a) 5µm × 5µm and 5µm x 5µm, (b) 20µm x 1µm and 1µm × 20µm, (c) 1µm × 85µm and 4µm × 60µm, and (d) 1µm × 100µm and 1µm x 130µm.

To illustrate different trends observed in Z_{12}, the cross-coupling impedances obtained from EPIC simulations for four different contact geometries is shown in Figure 3.10.

In the case of misaligned contacts, Z_{12} does not exhibit a consistent exponential decrease with respect to GMD, especially for long contacts ($L > 50\mu m$) at close separations. The Z_{12} plot with $X_{ee} = 2\mu m$ portrays near field effects where Z_{12} is not an exponential function of the GMD for long contacts. The Z_{12} plot when X_{ee} is very large ($50\mu m$), exhibits far field effects where Z_{12} is an exponential function with respect to the GMD.

From the above observations, the behavior of Z_{12} is differentiated based on relative positions of contacts in the following two ways: A contact within the proximity of another contact and a contact not in the proximity of the other contact. Figure 3.11 shows these definitions.
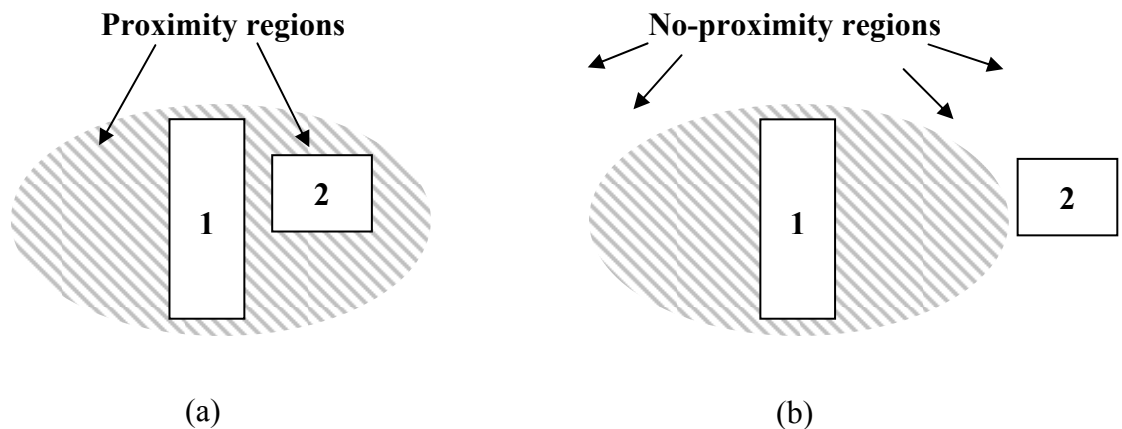
Figure 3.11. Relative positions of Contact 2 with respect to Contact 1 (a) Contact 2 in the proximity region of Contact 1. (b) Contact 2 in the no-proximity region of Contact1.

The following is a summary based on an analysis of the trends in the cross-coupling impedances for the entire geometric data set:

i.   The cross-coupling impedance is exponential with respect to the GMD for all cases when the second contact lies out of the proximity region of the first contact. This region is portrayed in Figure 3.11(b).

ii.   The deviation from the exponential behavior is prominent for long contacts (L > 50µm) that are within the proximity region as marked in Figure 3.11(a).

3.4.2.1. Z_{12} model for contact cases that lie outside each other's proximity region

Equation (3.5) developed in the previous section is applied to model the mutual impedance between contact geometries that are located outside each contact's proximity region (Figure 3.12).
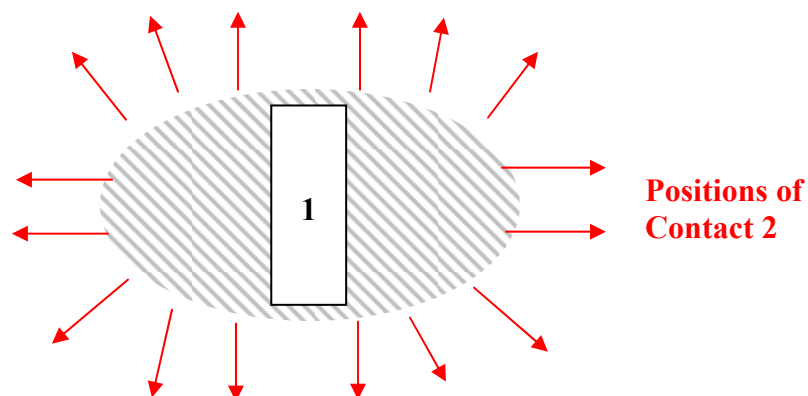
Figure 3.12. Positions for Contact 2 with respect to Contact 1 that are outside the proximity region of Contact 1.

The relative errors between the EPIC simulation results and the GMD model are within ±10% for the same range of contact dimensions as quantified in Section 3.4.1 (Figures 3.13 and 3.14).
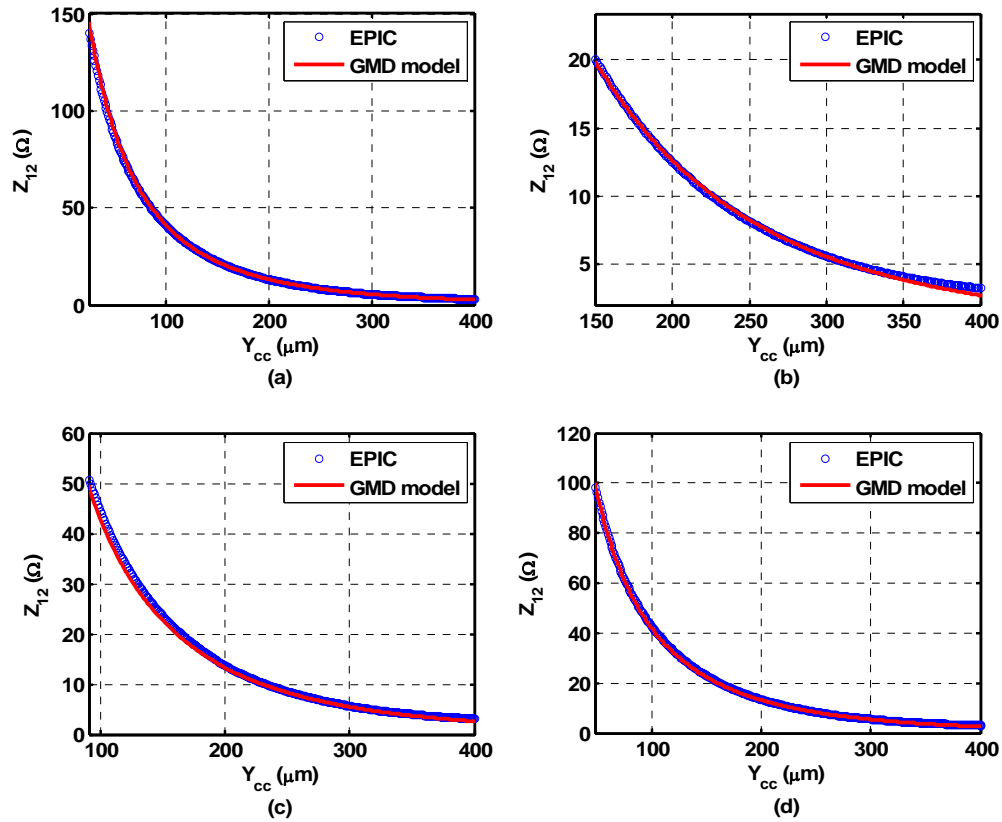
Figure 3.13. Comparison of the GMD model with EPIC simulations for cases placed in the no-proximity region with $X_{ee} = 4\mu m$. The contact dimensions are (a) 5µm×5µm and 5µm×5µm, (b) 20µm×1µm and 1µm×20µm, (c) 1µm×85µm and 4µm×60µm, and (d) 1µm×100µm and 1µm×130µm.

Figure 3.14. Comparison of the GMD model with EPIC simulations for cases placed in the no-proximity region with $X_{ee} = 50\mu m$. The contact dimensions are (a) $5\mu m \times 5\mu m$ and $5\mu m \times 5\mu m$, (b) $20\mu m \times 1\mu m$ and $1\mu m \times 20\mu m$, (c) $1\mu m \times 85\mu m$ and $4\mu m \times 60\mu m$, and (d) $1\mu m \times 100\mu m$ and $1\mu m \times 130\mu m$.

3.4.2.2. Z_{12} model for contact cases that lie inside the proximity region

For the cases where a contact is in the proximity region of another contact, Z_{12} is not an exponential function of the GMD. To model the behavior of Z_{12} in these regions, an analysis was carried out with different contact geometries and orientations. It was found that the Z_{12} is a function of not only the GMD but also the overlap-length inside the proximity region. The idea of overlap-length is made clear in Figure 3.15.
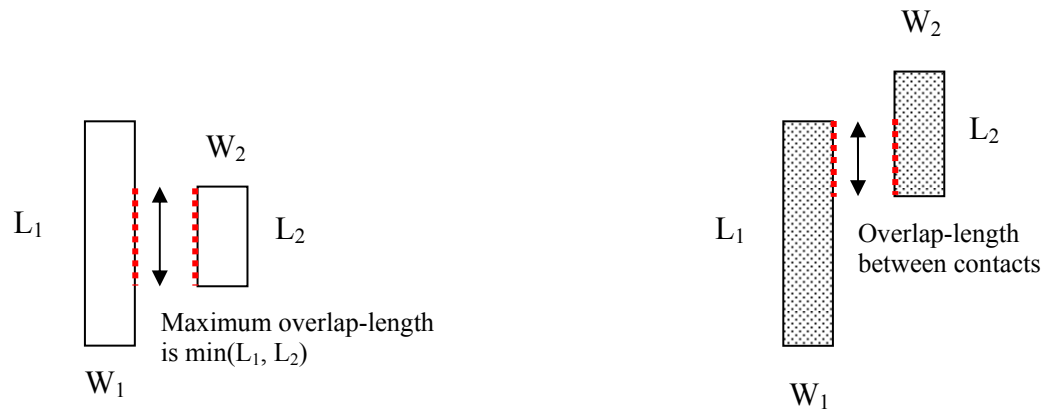
Figure 3.15. Overlap-length definitions.

Two examples are considered, to support the above finding. In each example, one contact is placed in the center of the die, and the other contact is separated by increasing and decreasing Y_{cc} with a constant X_{ee} (Figure 3.16). In the first example, the length of the 2nd contact is small compared to the length of the 1st contact. The overlap-length changes only when the 2nd contact is near the corners of the first one (Figure 3.17(c)). The cross-coupling impedance Z_{12} behaves in the same manner (Figure 3.17(a)). In the second case, the lengths of the contacts are comparable, and the overlap-length decreases linearly with the maximum being at $Y_{cc}=0$ (Figure 3.17(d)). Z_{12} follows the same trend as shown in Figure 3.17(b).

Example 1: 1μm×110μm
and 5μm ×27μm

Example 2: 1μm ×100μm
and 1μm ×100 μm
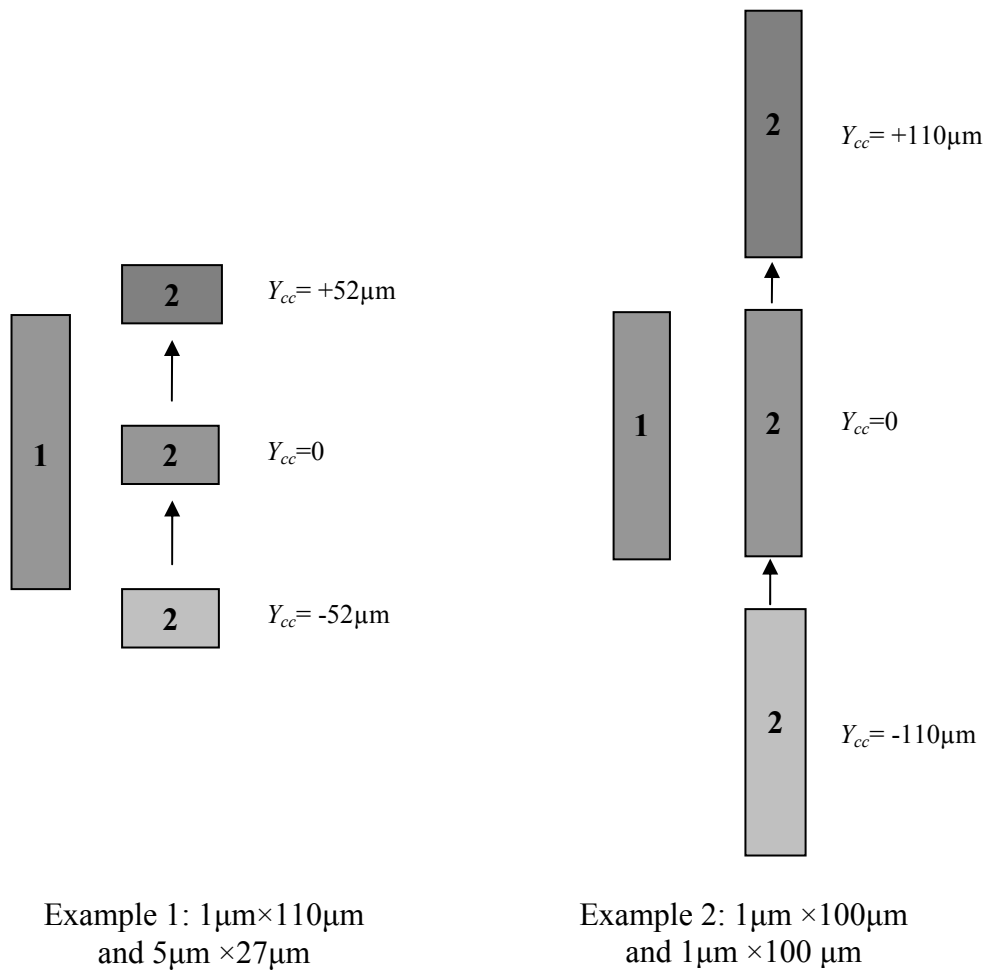
Figure 3.16. Relative positions for Contact 2 with respect to Contact 1 as Y_{cc} is varied.
(Figures not drawn to scale)
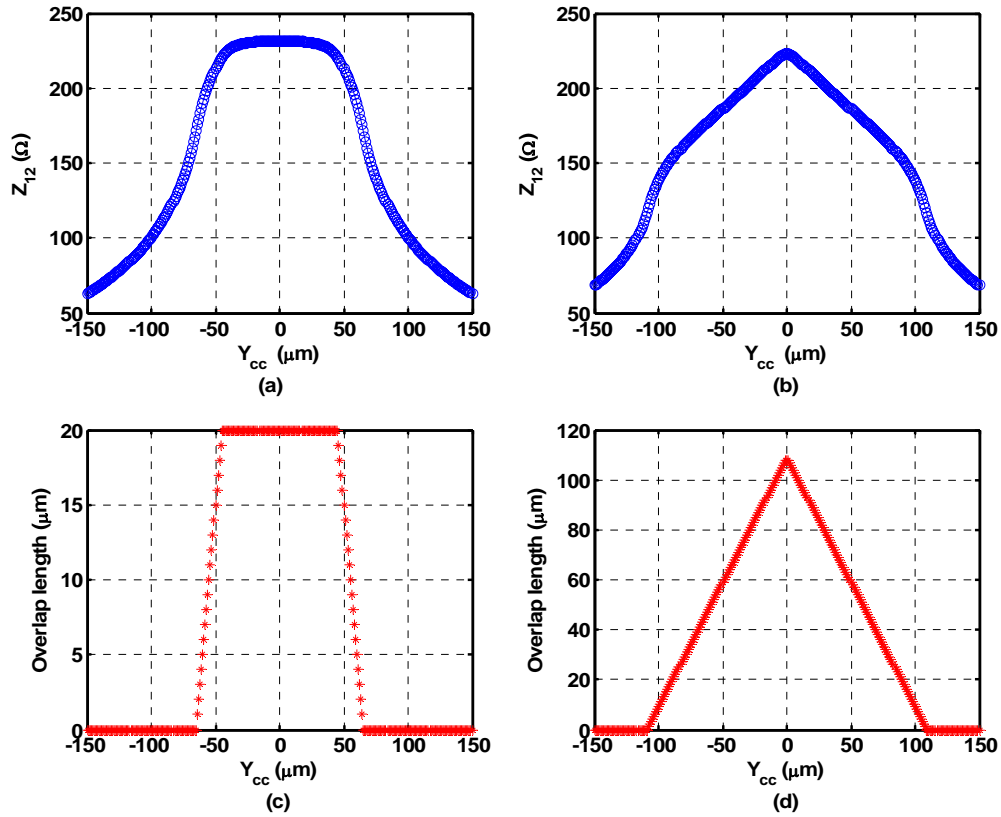
Figure 3.17. The behavior of Z_{12} and the overlap-length when Y_{cc} is increased. (a) Z_{12} from EPIC simulations for Example 1. (b) Z_{12} from EPIC simulations for Example 2. (c) Corresponding overlap-length behavior for Example 1. (d) Corresponding overlap-length behavior for Example 2.

Clearly Z_{12} depends on the overlap-length in the proximity region. The point of maximum overlap is at $Y_{cc}=0$. The impedance at $Y_{cc}=0$ is computed using Equation (3.5), since the exponential behavior of Z_{12} is guaranteed when X_{ee} is increased, keeping $Y_{cc} = 0$ (Section 3.4.1). In order to model the behavior of Z_{12} with proximity effects, Equation (3.5) is modified to include a normalized overlap-length term.

The equation for the improved model is:

$$Z_{12} = Z_{12(c-c)} \left(\frac{overlap\_length}{maximum\_overlap\_length} \right)^{c_1} \tag{3.6}$$

where c_1 is a function of the geometry and $Z_{12(c-c)}$ is the cross-coupling impedance from Equation (3.5). It is to be noted that at $Y_{cc} = 0$, the overlap is at its maximum value and *overlap_length* equals *maximum_overlap_length*. Hence Equation (3.6) reduces to Equation (3.5).

Equation (3.6) models the behavior of Z_{12} in cases where the second contact is in the proximity region of the first contact. The performance of the improved model (Equation (3.6)) is compared with the original GMD model (Equation (3.5)) and with EPIC simulations. Results for four contact cases with different X_{ee} values are presented in Figure 3.18.

The plots confirm the earlier observation that the original GMD model suffers from accuracy issues (relative errors > 15%) at close separations. On the other hand, the improved model has relative errors that are less than 10%. The relative errors in the improved model increase for X_{ee} less than 2μm.

There is a discontinuity in the model equations in the region of transition where the improved model is switched to the GMD model. The switching of the improved model to the GMD model is required to describe the impedances in the proximity region and no-proximity regions, respectively. Standard linear or exponential smoothing techniques were not efficient in making the transition smooth between the two model equations and the possibility of using more advanced smoothing functions remains a

direction for future research. The discontinuity causes more errors compared to the GMD model for a few cases as shown in Figure 3.18(a).
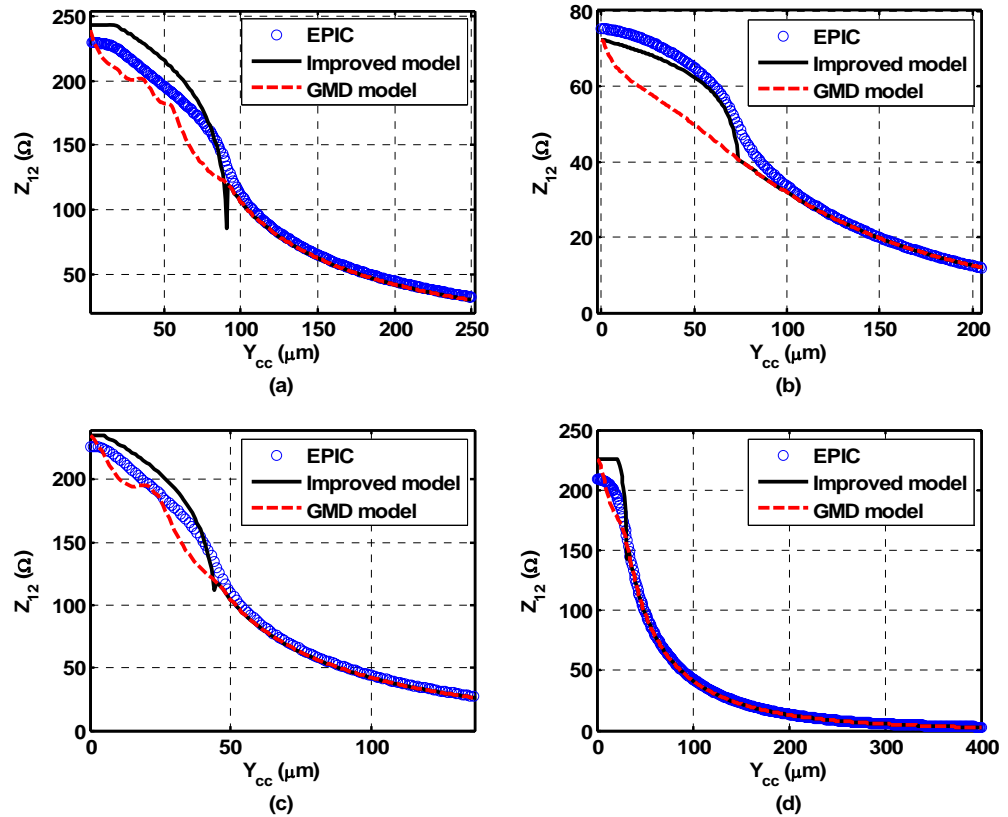
Figure 3.18. Comparison of the improved Z_{12} model equation with model Equation (3.5) and EPIC for contact dimensions (a) 1μm×110μm and 5μm×73μm (X_{ee}=2μm), (b) 150μm×150μm and 150μm×150μm (X_{ee}=4μm), (c) 3μm×80μm and 4μm×100μm (X_{ee}=4μm), and (d) 1μm×110μm and 5μm×20μm (X_{ee}=10μm).

The next step is to model c_1 as a function of the geometry and identify the proximity regions where the improved model equation is applicable. The approach to modeling c_1 is similar to that of a_1 in Section 3.4.1. From the experiments above, c_1 is extracted for various contact cases at a particular value of X_{ee}. The values are shown in Figure 3.19(a). For contacts having small lengths, the proximity effects are negligible.

Hence, c_1 should be such that Equation (3.6) reduces to Equation (3.5) for contacts with small lengths. A logarithmic function is used to model c_1 to capture this behavior.

$$c_1 = \log\left(k_4\left(\frac{sum\_of\_lengths}{sum\_of\_widths^{k_5}} \right) + 1 \right) \tag{3.7}$$

where k_4 and k_5 are process constants with values $k_4=0.002$ $(\mu m)^{-0.75}$ and $k_5=0.25$. For contacts with small lengths, c_1 reduces to 0.
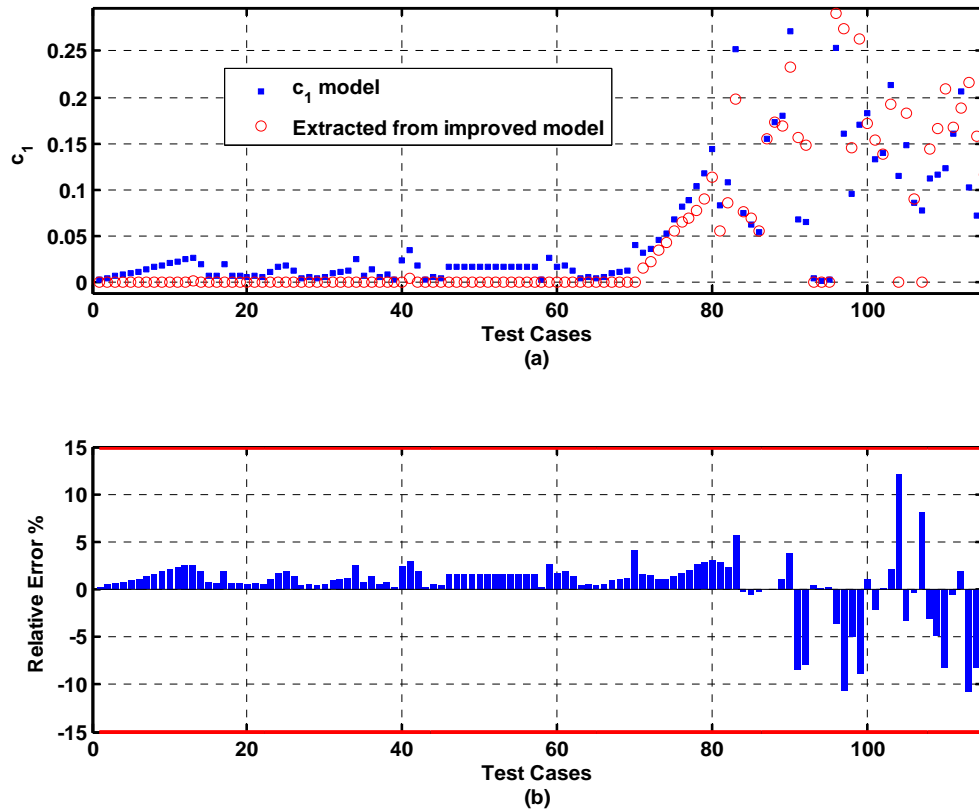
Figure 3.19. Accuracy of the c_1 model for all contact geometries. (a) Comparison of the c_1 model with the improved model extracted values. (b) Relative errors for the c_1 model compared with the improved model extracted values.

The accuracy of this model is determined by comparing the c_1 values computed from Equation (3.7) with the values extracted while developing the improved model. Figure 3.19(b) shows that the relative errors for this c_1 model are within 12%.

Next the region of proximity is considered. The first observation is that, the proximity region (Figure 3.11(a)) is larger for longer contacts. For example, a set of square contacts with dimension 100μm may experience proximity effects at a separation of 50μm. On the other hand, contacts with dimension 5μm may not experience proximity effects at the same separation. The ratio of the sum of the lengths (L_1+L_2) to the shortest distance between the edges of the contacts, X_{ee}, is used to quantify these regions. The relative error of the GMD model was observed to be higher than 15%, due to proximity effects, when this ratio was greater than 10. Consequently, the improved model equation is used whenever the ratio exceeds 10.

The complete cross-coupling impedance model formulation is given by the set of equations:

$$Z_{12} = a_1 e^{-k_3\sqrt{gmd}} \qquad \text{if contacts are not within the proximity region} \tag{3.8}$$

$$Z_{12} = a_1 e^{-k_3\sqrt{gmd_{c-c}}} \left(\frac{overlap\_length}{maximum\_overlap\_length}\right)^{c_1} \quad \text{if contacts are within the proximity}$$

region (3.9)

The gmd_{c-c} is the geometric mean distance between contacts when their centers are aligned. The proximity effects in modeling Z_{12} occur when the ratio of the sum of contact lengths (L_1+L_2) to the shortest distance between the edges of the contacts, X_{ee} is

greater than 10. The final comparison of the entire macromodel with the EPIC simulated

values is illustrated in Figure 3.20.
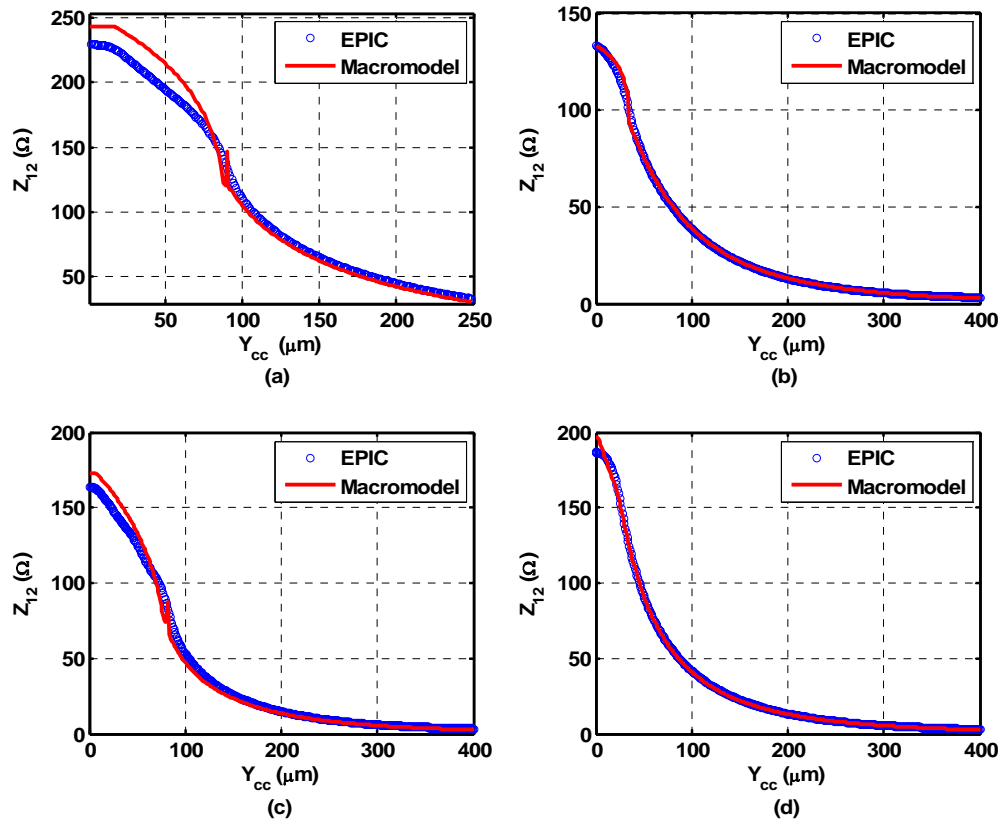
Figure 3.20. Comparison of Z_{12} macromodel with EPIC simulation results. The contact dimensions are (a) 1µm×110µm and 5µm×108µm, (b) 70µm×70µm and 70µm×70µm, (c) 6µm×180µm and 5µm×150µm, and (d) 30µm×6µm and 6µm×90µm.

The complete cross-coupling impedance model requires a total of 5 process

constants. The relative errors between the model and EPIC simulations are within ±15%

for a large set of dimensions and separations.

3.5. Self-impedance (Z_{11}) model

The self-impedance models presented in [7] and [9] are functions of the area and perimeter of a contact and do not account for any interaction from the neighboring contacts. At small separations, the self-impedance of a contact is affected by the surrounding contacts [16]. Figure 3.21 shows the variation of the self-impedance with separation for four different square contacts.
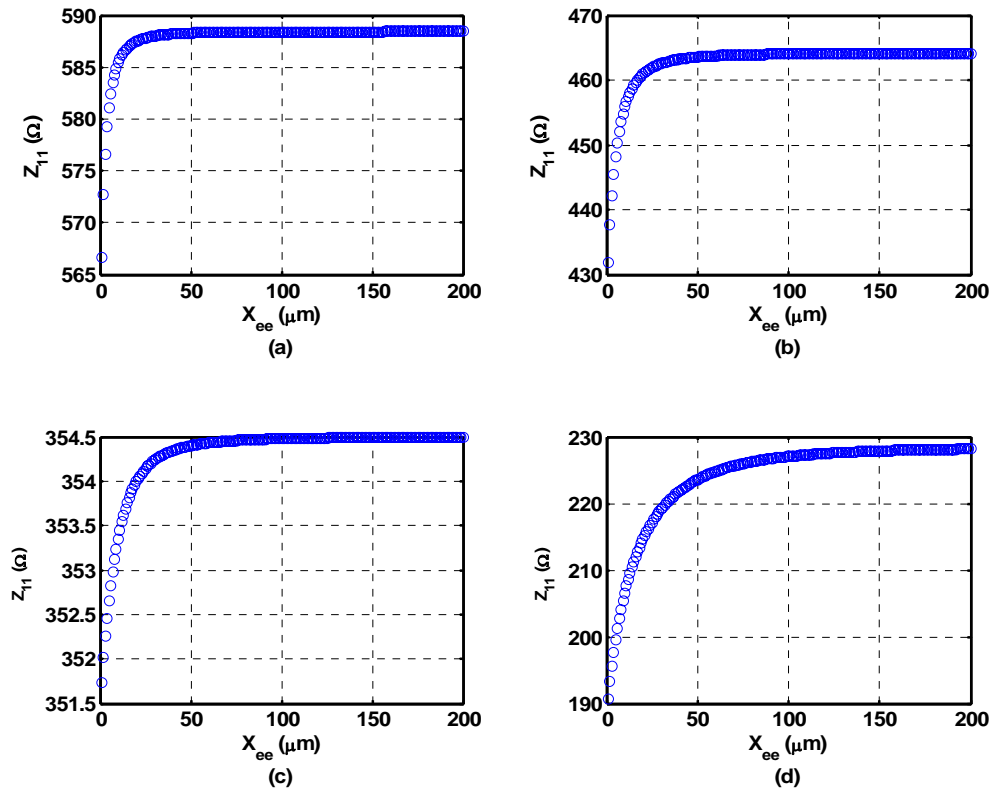
Figure 3.21. Examples to show that Z_{11} deviates from constant values for small separations. The contact sizes are (a) 5µm×5µm and 5µm×5µm, (b) 10µm×10µm and 10µm×10µm, (c) 20µm ×20µm and 20µm×20µm, and (d) 50µm×50µm and 50µm×50µm.

It is clear from the plots that Z_{11} decreases with a decrease in separation due to the presence of the other contact. As the separation increases, this effect diminishes, and Z_{11} approaches a constant value which is a function of the contact's geometry.

As a first step, the Z_{11} (or Z_{22}) are modeled assuming there is no influence from the surrounding contacts. This is consistent with the assumption that Z-parameters are independent of other contacts (Section 2.2). EPIC simulations were performed for the set of contact geometries and self-impedance values were extracted. The resulting self-impedance values are modeled using the contact area and perimeter information as:

$$Z_{11} = \frac{1}{\alpha_1(area) + \alpha_2(perimeter)^{\alpha_3} + \alpha_4} \qquad (3.10)$$

where $\alpha_1, \alpha_2, \alpha_3$ and α_4 are process constants. The parameter α_3 is introduced to increase the accuracy of previous models [7], [9]. Without α_3 the model gives errors greater than 20% and as high as 40% when compared to EPIC simulations results. However, the improved model matches the simulation results with relative errors less than 8%, as depicted in Figure 3.22. The process constants for this model are:

$\alpha_1 = 9.5 \times 10^{-8} (\mu m)^{-2} \Omega^{-1}$ $\qquad$ $\alpha_2 = 3 \times 10^{-6} (\mu m)^{-0.5} \Omega^{-1}$ $\qquad$ $\alpha_3 = 0.5$

$\alpha_4 = 4.6 \times 10^{-4} \Omega^{-1}$

Proximity effects due to the neighboring contacts for the self-impedance are described in Chapter 4.
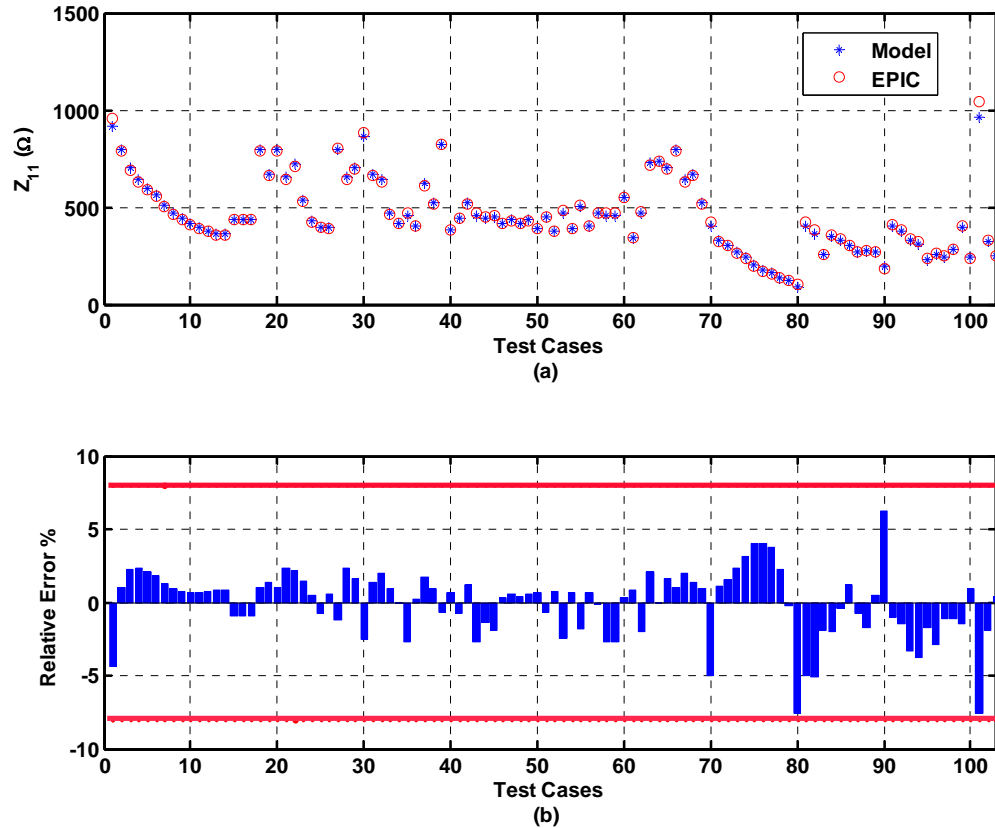
Figure 3.22. Z_{11} model as a function of the contact geometry. (a) Comparison of Z_{11} model with EPIC values. (b) Relative errors for the Z_{11} model compared with EPIC values.

3.6. Summary of the macromodel development

This chapter was dedicated to the analysis and modeling of Z-parameters for two contacts in a lightly doped substrate. The GMD model was improved using a simple overlap-length function to eliminate the inaccuracies caused by the GMD at close separations. This is crucial as practical layouts (both analog and digital) consist of closely spaced long contacts. The self-impedance model was also improved using an extra

process parameter. The self-impedance model does not account for the proximity of neighboring contacts. The model equations (Equations (3.8), (3.9), (3.10)) developed in this chapter require nine process constants and have a reasonable accuracy for a very large set of layout geometries and separations.

The geometric data set for the model parameter extraction has been optimized in Appendix E. The optimization of the data set is required for efficient extraction of model parameters when the macromodel equations are needed for different processes.

4. PANELING APPROACH TO OVERCOME MACROMODEL LIMITATIONS

In the previous chapter, the lightly doped substrate was characterized based on two-port Z-parameters. The self-impedance was assumed to be independent of the surrounding contacts. However, this assumption is not valid, and the self-impedance is affected by surrounding contacts placed at close separations. This chapter examines a paneling approach for incorporating these proximity effects in the self-impedance model. In addition, the paneling approach is applied with the GMD model for modeling mutual impedances. This is to check if the GMD limitations are overcome without using the improved model. Once proximity effects are accounted for in the two-port model, the macromodel with paneling can be easily extended for multiple contacts.

4.1. The need for paneling

By definition, the Z or open-circuit parameters are independent of the neighboring contacts. However, proximity or presence of near-by contacts affects the self-impedance values. Figure 4.1 illustrates the variation in the self impedance for closely placed contacts. The plots show normalized self-impedance values for different contact sizes for a range of separations. It is observed that small contacts exhibit proximity effects at smaller separations and large contacts for much larger separations, i.e., greater than 100μm for two 100μm×100μm contacts. Therefore, the size of the contacts as well as the separations have to be considered for proximity effects. For this reason, the previous Z-

parameter based model is not adequate and the influence of the neighboring contacts on Z_{11} (or Z_{22}) has to be incorporated.

It is tedious to include the influence of neighboring contacts while modeling the self-impedances for an N-contact network. The impedance of an N-port is represented by an N×N impedance matrix **Z**. Due to contact proximity each diagonal element (Z_{ii} or self-impedance) of **Z** will depend on the other N-1 contacts. This complicates the dependencies of Z_{ii}. A paneling approach has been suggested in [17] to model such effects. This idea was based on the work presented in [18]. The paneling approach is also used in this thesis. A ±5-10% variation in the self-impedance values is assumed to be acceptable for small contacts.
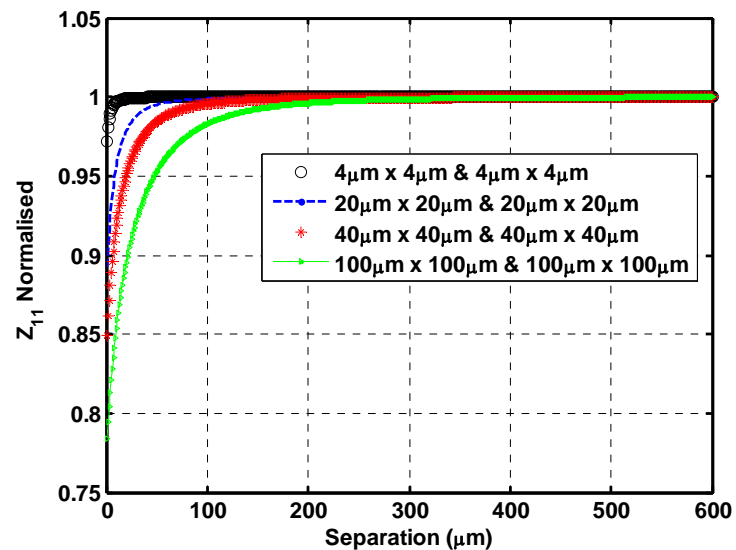
Figure 4.1 Influence of proximity effects on self-impedance values.

4.2. The paneling approach

The paneling approach involves dividing the contacts into panels. The panels are assumed to be equipotential and have a uniform current density. The paneling algorithm has been developed for a general case where the contacts have been divided along both the length and width as shown in Figure 4.2.

Contact 1 divided into *a* panels   Contact 2 divided into *b* panels
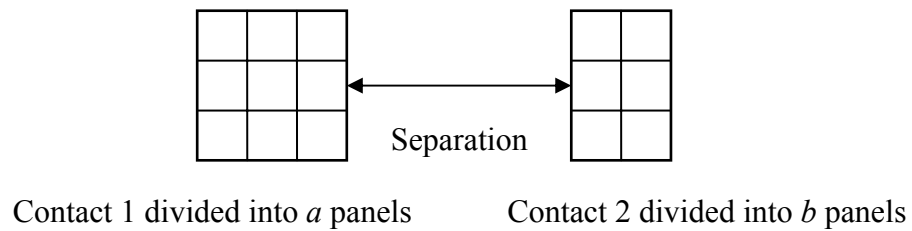
Figure 4.2. Panel division for 2 contacts.

The paneling algorithm steps are as follows:

Step 1: **Panel formation**

- Divide the contacts into *a* and *b* panels, respectively.

- Obtain the sizes and separations of panels based on geometric information to calculate the panel level **Z**-matrix ($\mathbf{Z_p}$).

Step 2: Calculating the panel level Z-matrix ($\mathbf{Z_p}$)

The calculation of the panel level $(a+b)\times(a+b)$ **Z**-matrix is shown in Figure 4.3. Based on the relative positions of panels, the panel level Z-parameters are calculated using the macromodel equations (Equation (3.8), Equation (3.9), and Equation (3.10)).

a and *b* panels
from contacts

n=1, m=1

No — n=m? — Yes

n and m
adjacent
panels ?

No — Yes

$\mathbf{Z_p(n,m)}=Z_{nm}$
(cross-coupling impedance)

$\mathbf{Z_p(n,m)}=$cross-coupling impedance assuming a small separation between adjacent panels

$\mathbf{Z_p(n,n)}=Z_{nn}=Z_{mm}$
(self-impedance)

m=m+1

Yes — m> (a+b) ? — No

n=n+1

n> (a+b) ? — No

Yes

Output = $\mathbf{Z_p}$ → Stop
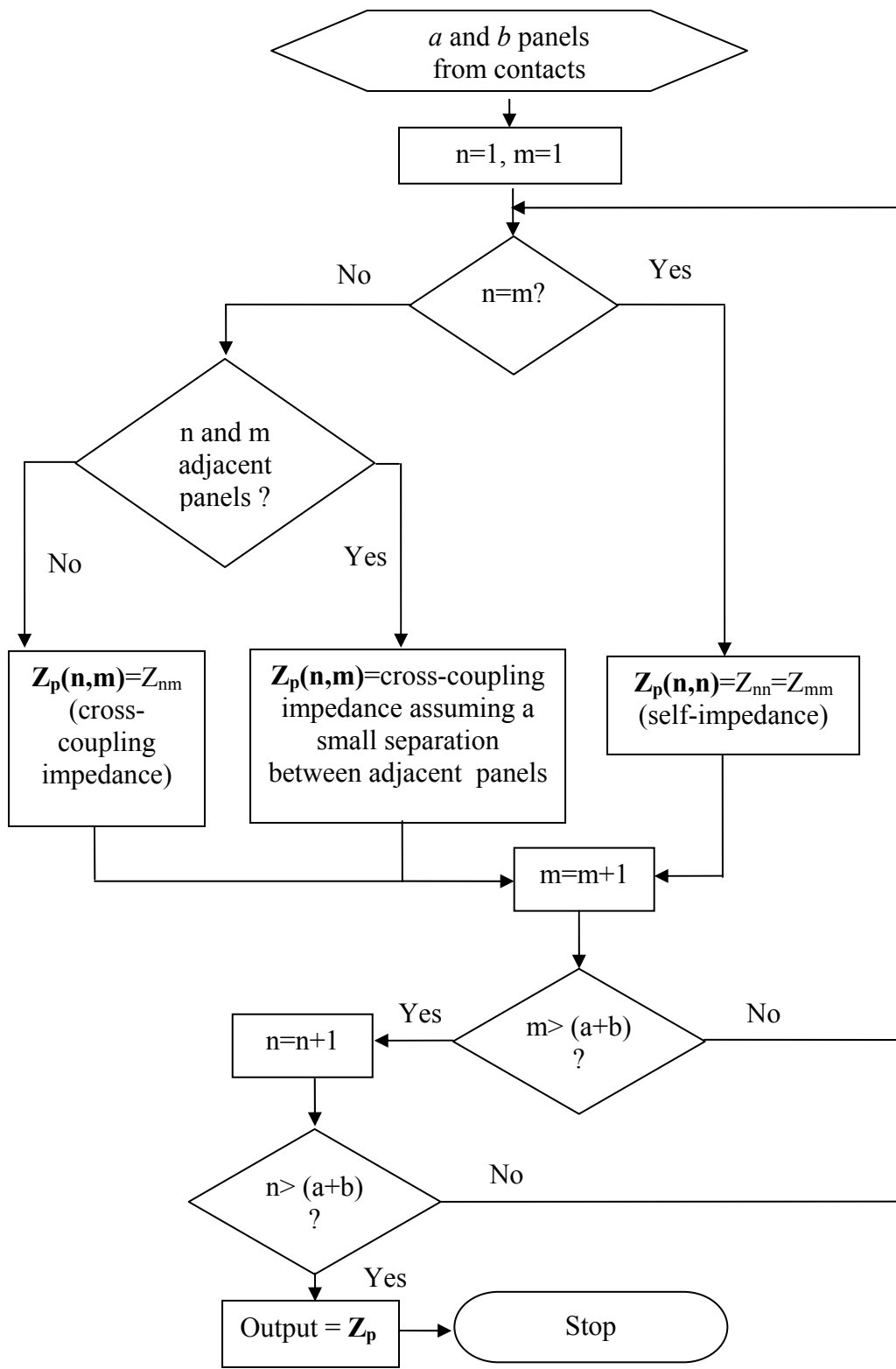
Figure 4.3. Flowchart for $\mathbf{Z_p}$ calculation.

Step 3: Calculation of the 2-port Z-matrix

- $\mathbf{Y_p} = \text{inv}(\mathbf{Z_p})$; The structure of this admittance matrix is as follows:

$$Y_p = \begin{bmatrix} Y_{1,1} & \cdot & \cdot & \cdot & \cdot & \cdot & \cdot & Y_{1,(a+b)} \\ \cdot & \cdot & \cdot & \cdot & \cdot & \cdot & & \cdot \\ \cdot & \cdot & \cdot & \cdot & \cdot & \cdot & & \cdot \\ Y_{a,1} & \cdot & \cdot & \cdot & \cdot & \cdot & & Y_{a,(a+b)} \\ Y_{(a+1),1} & \cdot & \cdot & \cdot & \cdot & \cdot & & Y_{(a+1),(a+b)} \\ \cdot & \cdot & \cdot & \cdot & \cdot & \cdot & & \cdot \\ \cdot & \cdot & \cdot & \cdot & \cdot & \cdot & & \cdot \\ Y_{(a+b),1} & \cdot & \cdot & \cdot & \cdot & \cdot & & Y_{(a+b),(a+b)} \end{bmatrix}$$

Admittances for all panels in Contact 1

Admittances for all panels in Contact 2
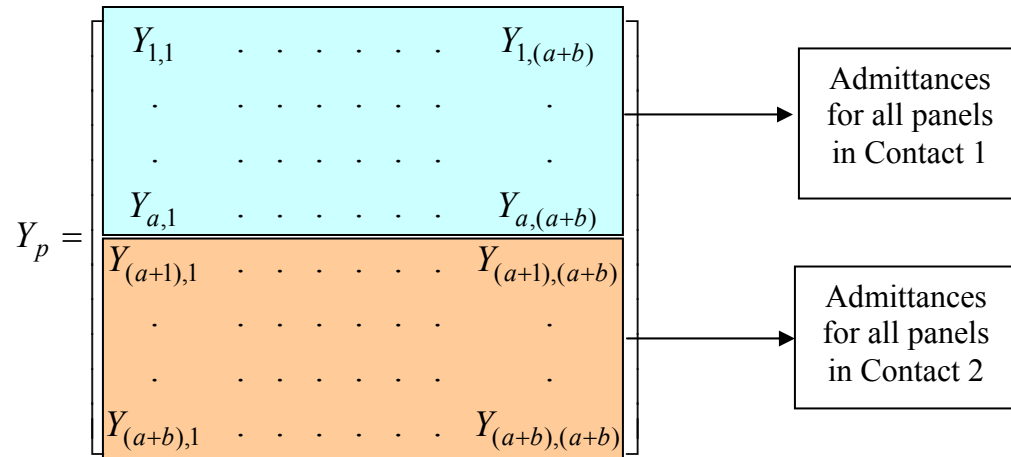
- **Calculating the 2-port R-matrix**

  a. The self resistance is calculated as below

$$\begin{bmatrix} R_{11} \\ R_{22} \end{bmatrix} = \begin{bmatrix} \displaystyle\sum_{k=1}^{a} \dfrac{1}{\displaystyle\sum_j Y_p(k,j)} \\[20pt] \displaystyle\sum_{k=a+1}^{a+b} \dfrac{1}{\displaystyle\sum_j Y_p(k,j)} \end{bmatrix}$$

  b. The mutual resistance is calculated as:

$$R_{mutual} = \frac{-1}{\displaystyle\sum_{i=1}^{a} \sum_{j=a+1}^{a+b} Y_p(i,j)}$$

  where $R_{mutual} = R_{12} = R_{21}$

The final R-matrix is:

$$R = \begin{bmatrix} R_{11} & R_{21} \\ R_{21} & R_{22} \end{bmatrix}$$

- Calculate 2-port **Y**-matrix from the above 2-port **R**-matrix

- Calculate 2-port **Z**-matrix by inverting the 2-port **Y**-matrix

Step-2 in the above approach requires that the macromodel be applied to adjacent panels. Before proceeding to validate our paneling approach, an explanation of how the macromodel can be applied to adjacent panels is provided.

4.2.1. The impedance model for adjacent panels (or contacts)

Since the two panels are adjacent to each other, they can be considered to be equipotential. Two adjacent contacts are represented in Figure 4.4(a) and the merged single contact is shown in Figure 4.4(b). The equivalent π-resistive network is represented in Figure 4.4(c).
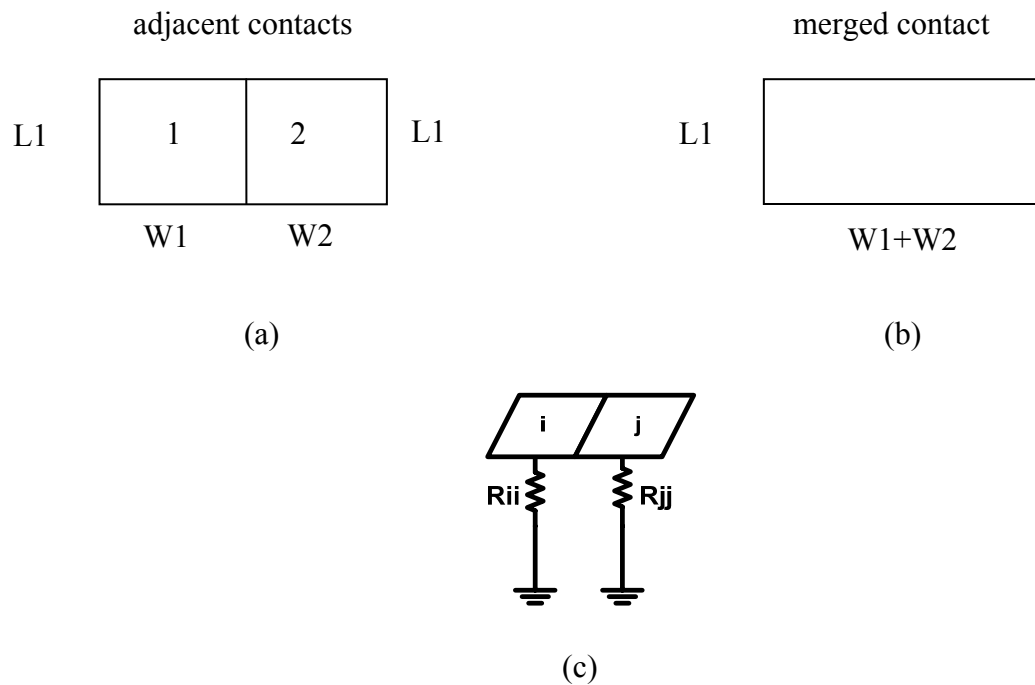
Figure 4.4. (a) Adjacent contacts. (b) Merged contact. (c) Resistive network for equipotential adjacent contacts.

The cross-coupling resistance, *Rij*, for the adjacent contact network is zero. Therefore, the two-port network reduces to a single port network:

$$Z_{ij} = \frac{R_{ii}R_{jj}}{R_{ii} + R_{jj} + R_{ij}} = \frac{R_{ii}R_{jj}}{R_{ii} + R_{jj}}\bigg|_{merged\_contacts} \tag{4.1}$$

and

$$Z_{ii} = R_{ii} \parallel (R_{jj} + R_{ij}) = R_{ii} \parallel R_{jj}\big|_{merged\_contacts} \tag{4.2}$$

Z_{ij}=Z_{ii}=Z=self-impedance of the overall merged contact

EPIC was used to perform simulations to determine the validity of the above equations, i.e., can two adjacent contacts (or panels) be considered as a merged contact (Figure 4.4). Many different geometric cases have been simulated, each with contacts having different dimensions. The separation between the adjacent contacts is varied between 0μm and 1μm. The results for two test cases are presented in Figure 4.5. It can be observed from the plots that the circuit parameters for adjacent contacts (Z_{12}, Z_{11}) do not match the self-impedance of the merged contact, Z_{merged} (at separation=0μm), which is not the expected behavior for adjacent contacts. EPIC does not consider two adjacent contacts as equivalent to a single merged contact contrary to Equations (4.1) and (4.2). This is clearly a problem with EPIC. For this reason, the adjacent panels or contacts are not modeled as a merged single contact. Instead, a 2-port network is extracted based on adjacent contacts being treated as very closely spaced contacts.
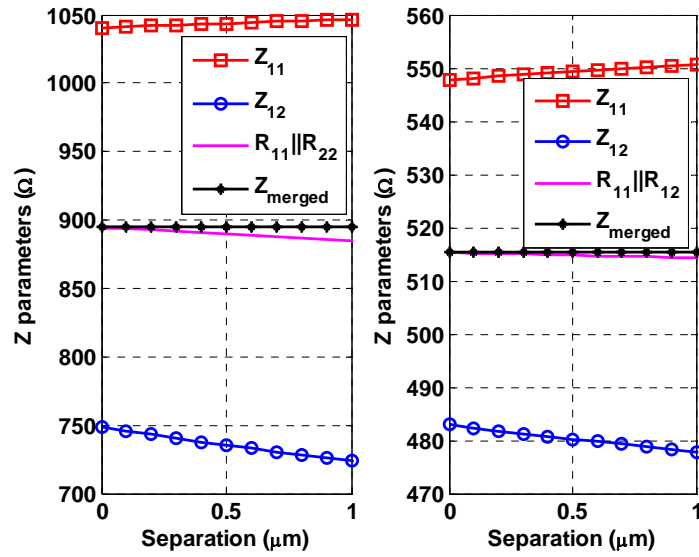
Figure 4.5. Comparison of Z-parameters from EPIC for merged single contacts with adjacent two contacts having contact dimensions (a) 1μm×1μm and 1μm×1μm, and (b) 5μm×5μm and 5μm×5μm.

Hence, the cross-coupling impedance for adjacent contacts can be approximated by $Z_{12\Delta}$. $Z_{12\Delta}$ denotes the cross-coupling impedance for 2 contacts placed at a very small separation (~ 0.5μm). The self impedances are given by Equation (3.10). The macromodel using small separations to model adjacent contacts, is shown to agree with relative errors less than ±15% with EPIC values. The results have been tabulated in Table 4.1 for a number of cases.

Table 4.1. Comparison of Z_{12} values from EPIC and the macromodel for very closely spaced panels/contacts (~ 0.5μm).

Contact Geometry	EPIC values (Ω)	Macromodel (Ω)	Error %
6μm×6μm and 6μm×6μm	451.19	385.73	14.5%
10μm×3μm and 3μm x16μm	407.63	366.44	10.0%
10μm×10μm and 10μm x10μm	380.78	342.22	10.0%
125μm×1μm and 125μm×1μm	115.13	108.76	5.5%
1μm×30μm and 2μm×2μm	403.85	394.98	2.2%
40μm×40μm and 40μm×40μm	204.09	202.8	0.063%

4.2.2. Paneling technique

While developing the paneling approach, it is important to establish the direction in which paneling is performed along the width of a contact, length of a contact, or both. Experiments to determine which paneling technique provides a better estimate of self-impedances have been carried out. Consider a pair of square contacts placed relative to each other, such that neighboring contacts affect the self-impedances (Section 4.1). The paneling algorithm was applied to calculate the Z-parameters. EPIC simulations were used to calculate the **Zp** matrix (Section 4.2), to accurately predict the self-impedances. The self-impedances from the paneling approach were compared to the self-impedances extracted directly from EPIC.

Paneling was carried out in two different ways. The contacts were divided into panels along the length (vertical paneling) and along the width (horizontal paneling).

Figure 4.6(b) and Figure 4.7(b) show that for the given pair of contacts, vertical paneling was more effective compared to horizontal paneling.

(a) (b)
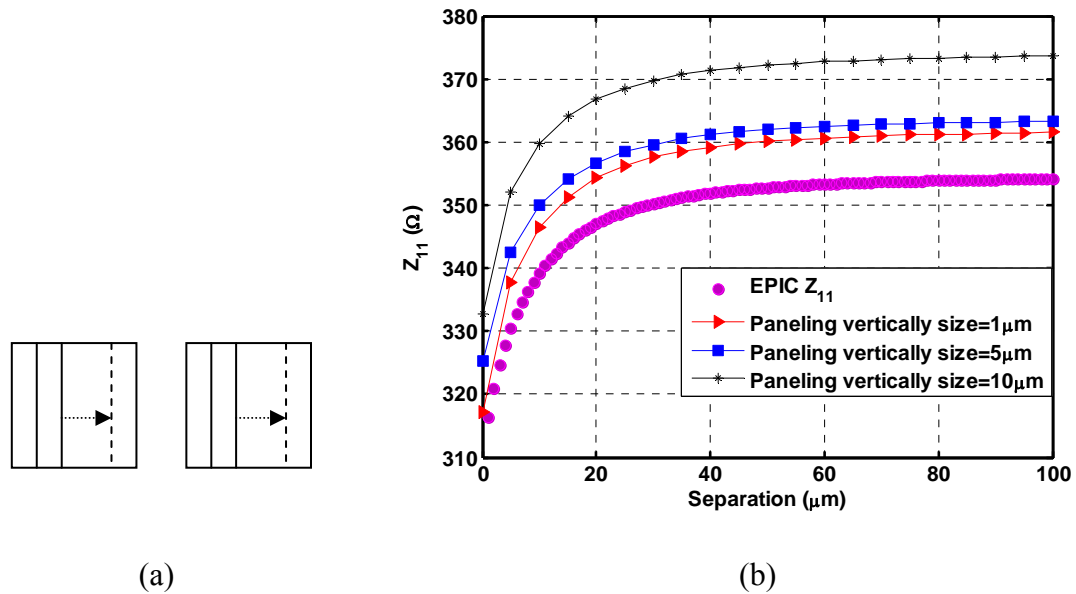
Figure 4.6. Effect of vertical paneling. (a) Paneling technique. (b) Comparison of Z_{11} obtained from varying panel sizes with reference Z_{11}, for a pair of 20µm×20µm contacts.

(a) (b)
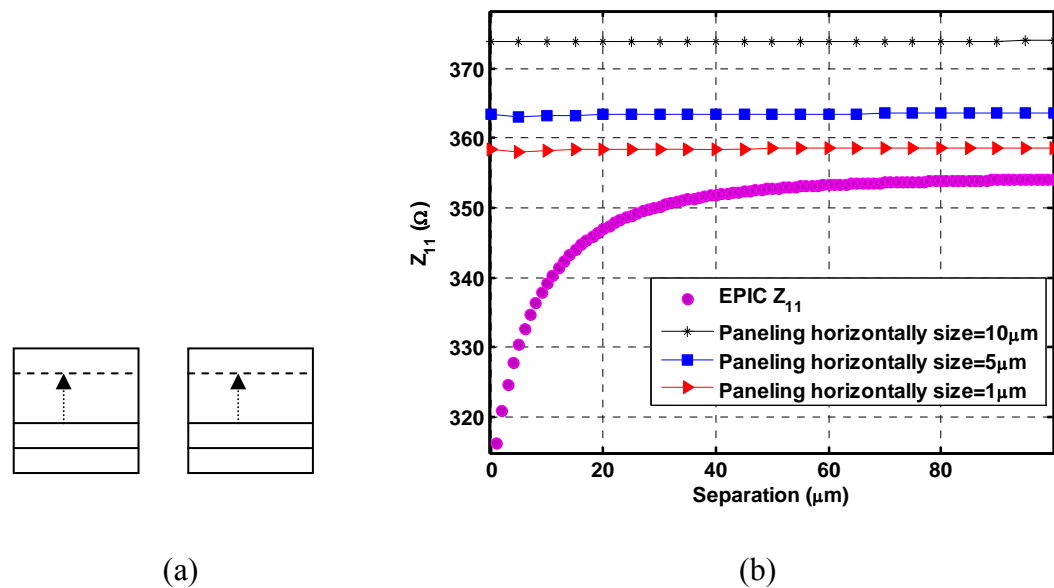
Figure 4.7. Effect of horizontal paneling. (a) Paneling technique. (b) Comparison of Z_{11} obtained from varying panel sizes with reference Z_{11}, for a pair of 20µm×20µm contacts.

Next consider two long skinny contacts. The paneling approach is applied to this example. EPIC simulations were carried out to extract the self-impedances. The results for horizontal and vertical paneling are shown in Figure 4.8. It was found that horizontal paneling was more effective compared to vertical paneling.
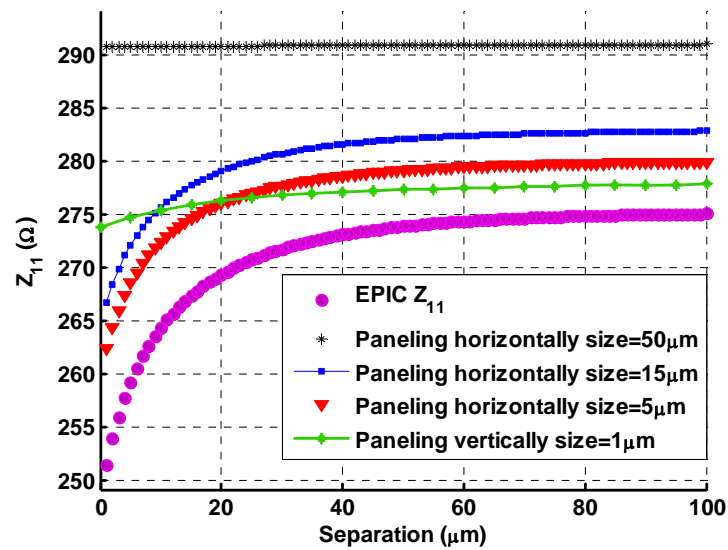
Figure 4.8. Horizontal and vertical paneling for long skinny contacts (3μm×80μm and 4μm×100μm).

Since the accuracy of the paneling technique is geometry dependent, simultaneous horizontal and vertical paneling was adopted. This makes the paneling algorithm more generic and applicable to a wide variety of contact geometries (Figure 4.2).

4.3. Macromodel with paneling for two-contact cases

The macromodel along with the paneling approach described in the previous section is applied to two-contact examples in this section. This is done to check if the proximity effects on the self-impedances are properly accounted for. Also, the paneling approach is applied to model mutual impedances using the GMD model to examine if the paneling approach can overcome the GMD limitations.

4.3.1. Self-impedance model with paneling

A simple example of a pair of square contacts is considered and the paneling approach is verified for different panel sizes. The modeled self impedances have been compared with the extracted impedance values from EPIC. Figure 4.9 shows that for panel sizes less than 5µm, Z_{11} modeled by the paneling approach does not tend towards the actual Z_{11} values extracted from EPIC.
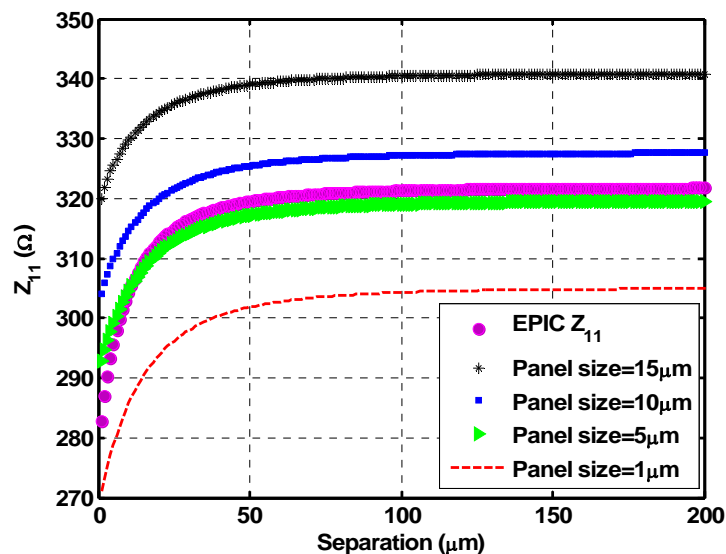
Figure 4.9. Macromodel with paneling applied to a set of 25µm×25µm contacts.

If the contacts are divided into more number of panels, the resulting Z_{11} should be more accurate. However, deviations from this expectation can be attributed to the inaccuracies in the macromodel, (for small dimensions at close separations) as stated in Section 3.4. Since the proximity effects are insignificant for small contacts, the paneling approach is applied with a minimum panel size of 5μm. The paneling approach was also applied to larger contacts, and the proximity effects were properly modeled. The results for four different contact geometries are shown in Figure 4.10.
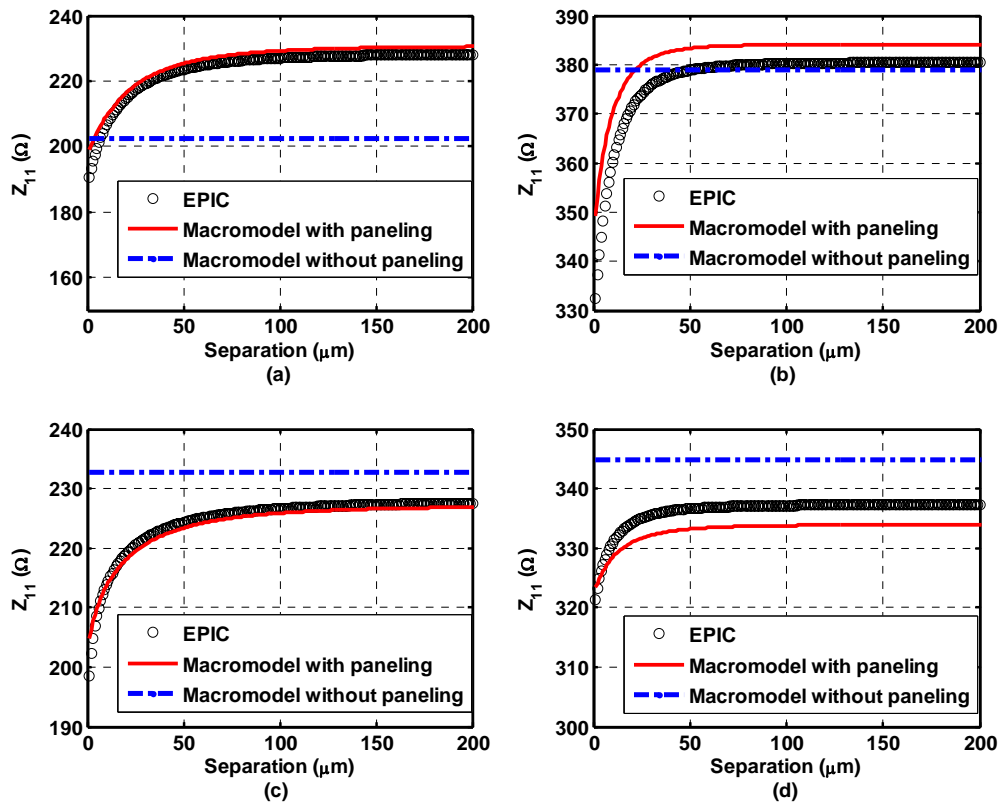
Figure 4.10. Macromodel Z_{11} with paneling compared with EPIC Z_{11} for contact dimensions (a) 50μm×50μm and 50μm×50μm, (b) 30μm×6μm and 6μm×90μm, (c) 125μm×1μm and 125μm×1μm, and (d) 25μm×20μm and 16μm×7μm.

The relative errors were observed to be less than 5% when compared to EPIC simulations. Clearly the macromodel applied without paneling gives errors greater than 15% when compared to EPIC simulations.

4.3.2 Mutual-impedance model with paneling

In the previous chapter, the GMD limitations for the mutual impedance model were overcome using an improved model (Equation (3.9)). In this chapter, the paneling approach is used in conjunction with the GMD model (Equation (3.8)) to check if the GMD limitations are resolved. The results for two examples are shown in Figure 4.11.
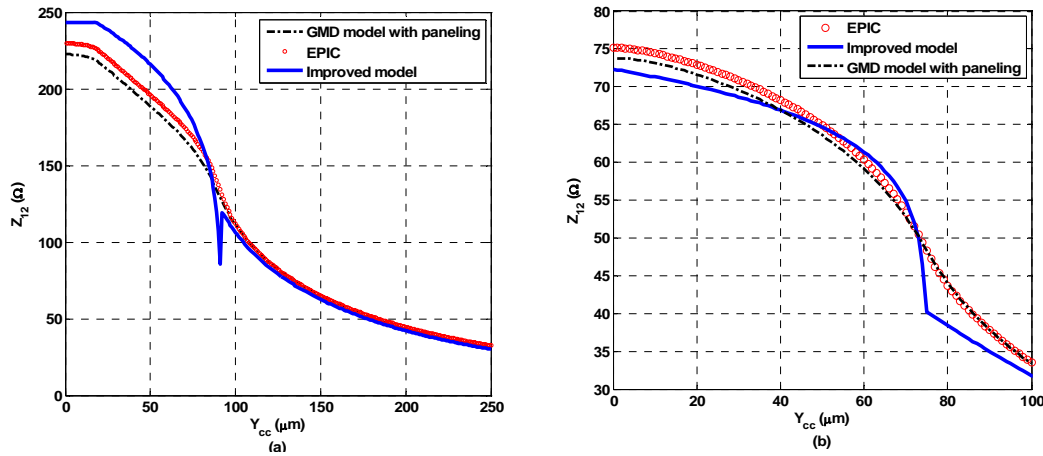
Figure 4.11. Macromodel Z_{12} with paneling compared with improved model and EPIC Z_{12} for contact dimensions (a) 1μm×110μm and 5μm×73μm placed at X_{ee}=2μm, and (b) 150μm×150μm and 150μm×150μm placed at X_{ee}=4μm.

Other geometric cases and proximity regions that required the application of the improved model were also tested with the GMD model in conjunction with paneling. It was found that the GMD model with paneling performed better than the improved model at the expense of computation time. For example, to acquire one value of Z_{12} for the pair of 150μm×150μm contacts, the macromodel with paneling (panel size=10μm) took 20

times more computation time than the macromodel without paneling. However, because of the paneling approach, relative errors for all cases were of the order of 10% when compared to EPIC simulations. There were no issues of discontinuity with this approach, when paneling is applied irrespective of the proximity region.

4.4. Extension of the model to multi-contact cases

As a first step in extending the model to multi-contact examples, a three-contact case is considered (Figure 4.12). Because of the presence of a third contact, the Z-parameters are affected by the neighboring contacts. The three contact substrate network is modeled using the macromodel in conjunction with paneling to account for the proximity of the third contact.

Examples of three contact Z-parameters are shown in Figure 4.13. Both the Z_{ii} and Z_{ij} are modeled with reasonable accuracy using the macromodel with paneling. The errors are within 10% for both the self and mutual impedances with this approach. The macromodel without paneling for the three contact example has errors as high as 60%.
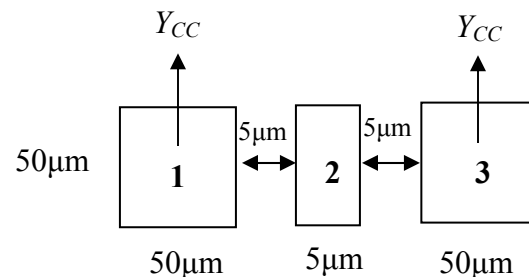
Figure 4.12. Example of 3 contacts separated by Y_{cc} distances.
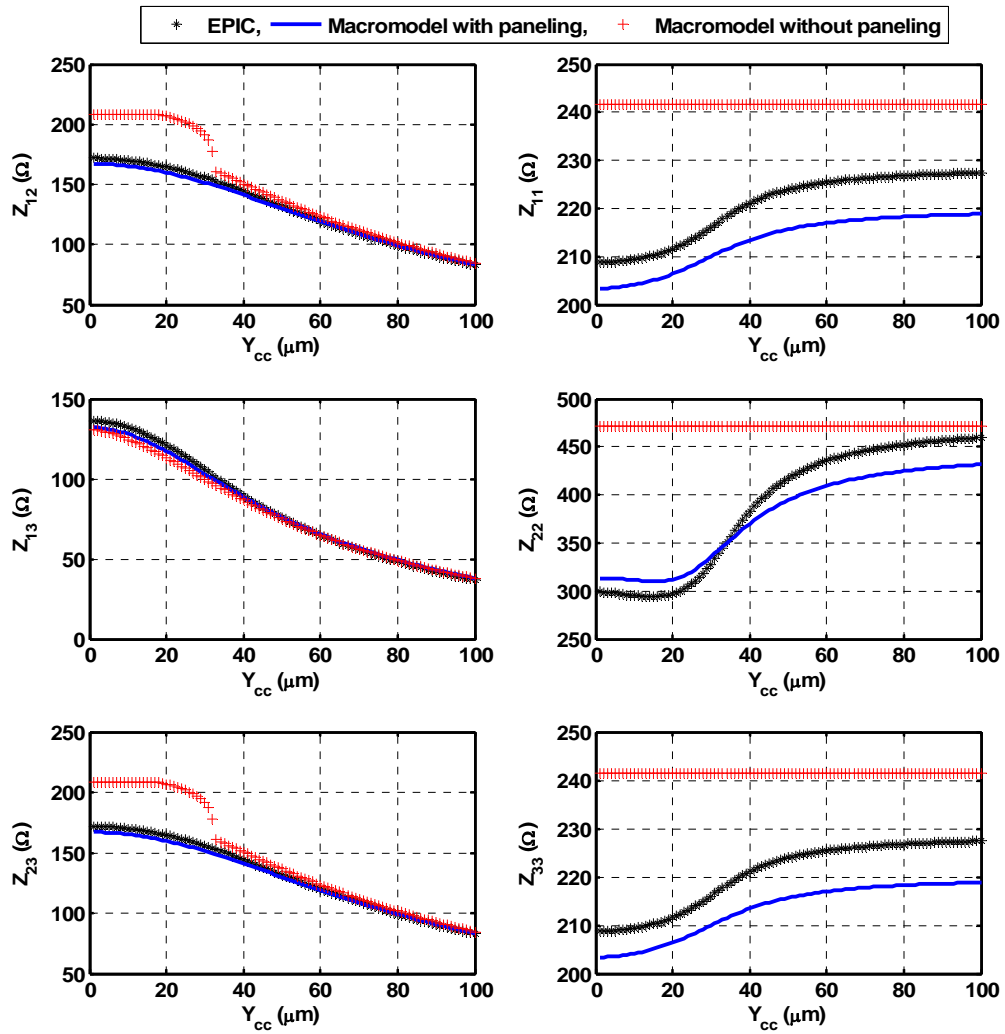
Figure 4.13. Comparison of the macromodel with paneling with EPIC simulations for a three contact example.

Another example of a multi-contact case is considered to evaluate the performance of the macromodel applied with paneling. Five square contacts with dimensions 50μm were placed on a 1mm×1mm die as shown in Figure 4.14. The X_{ee} separation was varied and the Z-parameters were extracted using EPIC.
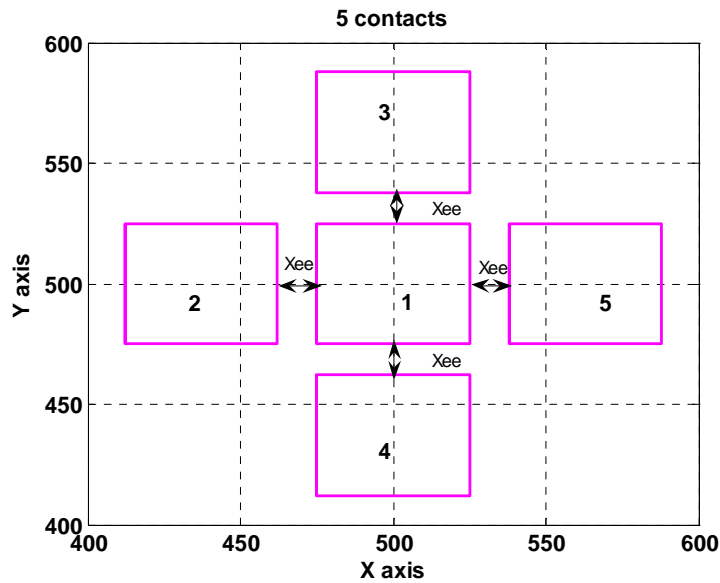
Figure 4.14. Layout of five square contacts with dimension 50μm in a 1mm×1mm die.

(a)   (b)
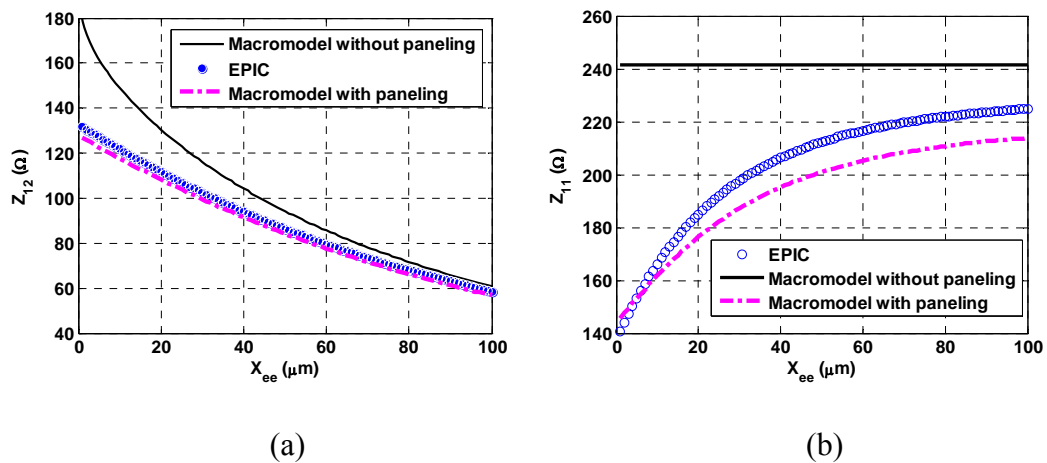
Figure 4.15. Comparison of the macromodel with paneling and macromodel without paneling with EPIC simulations for a five contact example. (a) Z_{12}. (b) Z_{11}.

Figure 4.16 presents the results for Z_{12} and Z_{11}. The comparison between macromodel (with and without paneling) and EPIC simulations are shown. It can be observed that the paneling approach is required to model the multi-contact Z-parameters correctly.

Based on the above analysis, it is clear that the paneling approach is important for extending the two-contact model to multiple contacts. In Chapter 5, a complex multi-contact example is validated using this extension. An outline of the advantages and pitfalls of the mutual-impedance modeling approaches is given in Table 4.2. The extra computation time for the paneling approach depends on the contact geometry and the panel sizes. A summary of the performance of the entire macromodel for two-contact and multi-contact cases is listed in Table 4.3.

Table 4.2. Comparison of improved Z_{12} model with the paneling approach.

Aspect	Improved Z_{12} model	GMD model with paneling
Relative errors compared to EPIC	within ±10-15%	within ±10%
Computation time (100 values)	< 2sec (both cases)	• 4 min (50μm×50μm and 50μm×50μm for a minimum panel size=10μm) • 20 sec (1μm×110μm and 5μm×73μm for a minimum panel size=5μm)
Discontinuity	Yes	No

Table 4.3. Summary of the model performances for two-contact and multi-contact cases.

Z- Models	2 Contacts		Multiple Contacts	
	w/o paneling	with paneling	w/o paneling	with paneling
Z_{12}: GMD Model Eq. (3.8)	Errors within ±10% when contacts out of proximity region. Errors >30% for contacts in proximity region.	Errors within ±10% for all cases	>20% errors	Errors within ±10% for all cases
Z_{12}: Improved Model Eq. (3.9)	Errors within ±15% for contacts in proximity region.	Not used[*]	>20% errors	Not used[*]
Z_{11}: Geometric Model Eq. (3.10)	Errors within ±8% for contacts having no proximity effects. >20% errors for contacts having proximity effects.	Errors within ±5% for all cases	>20% errors	Errors within ±5% for all cases

---

[*] The paneling approach uses a uniform panel size of 5μm. Hence, if the macromodel is used with paneling, the improved model is not required.

5. VALIDATION OF THE MACROMODEL FOR LIGHTLY DOPED SUBSTRATES

The macromodel developed in Chapter 3 is further validated for a different set of geometries and variations of the contact separation along the diagonal. Comparisons with existing measured Z-parameter values obtained for a 0.25µm CMOS process are also made. The application of the model (in conjunction with paneling) for simulating the substrate noise coupled to a 2.4GHz RF LNA from a stepped buffer is also presented.

5.1. Validation for a different data set

To further validate the macromodel, it is essential to show that it works for a data set that that was not considered during the model development phase.

Figure 5.1 presents sixteen test cases for validating the self-impedance model. The relative errors between the macromodel and EPIC simulations are within ±5%. Figure 5.2 compares the mutual impedance extracted from EPIC and the values predicted by the model for four different contact geometries. The model is in very good agreement with the EPIC extracted Z-parameters with relative errors within 10%.
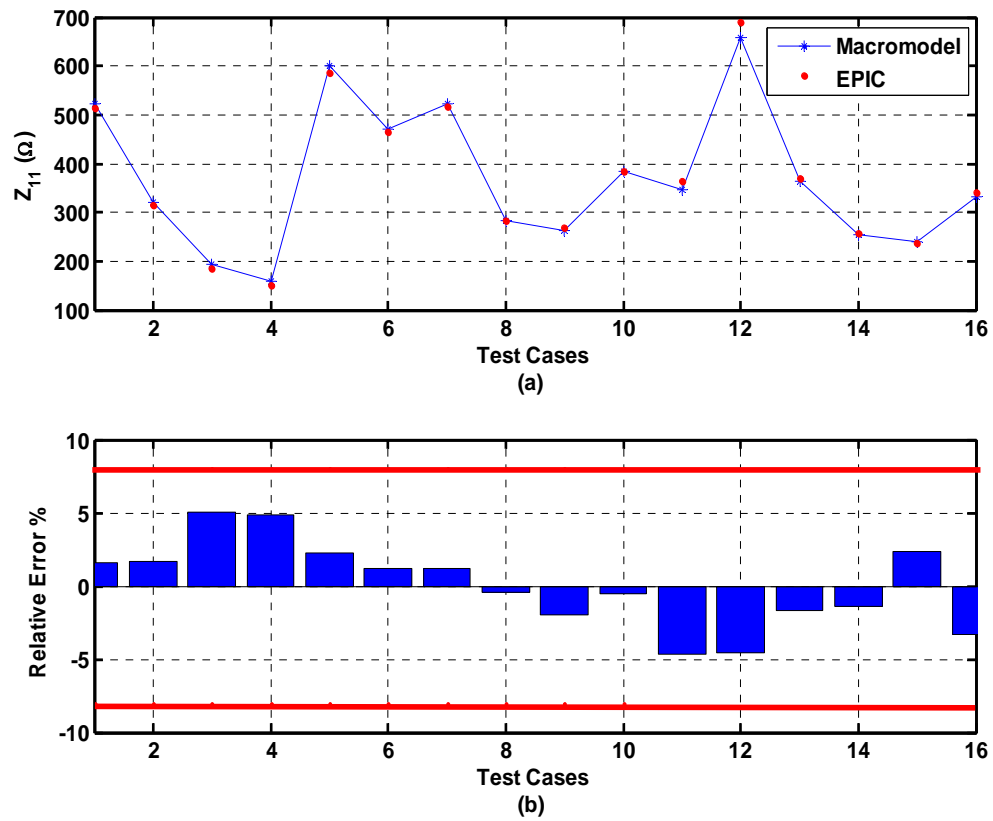
Figure 5.1. Validation of the self-impedance macromodel for different geometries. (a) Comparison of the Z_{11} model with EPIC values. (b) Relative errors for the Z_{11} model compared with EPIC values.
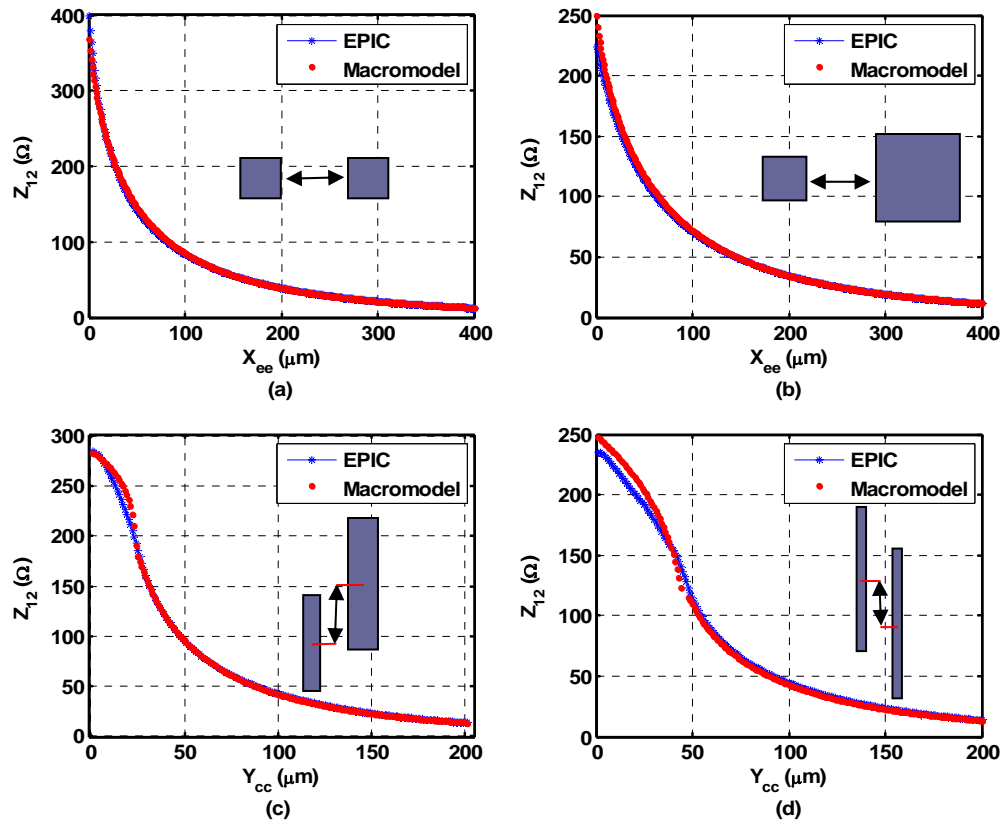
Figure 5.2. Validation of the cross-coupling impedance macromodel using different geometries for X_{ee} and Y_{cc} with contacts dimensions (a) 7.5µm×7.5µm and 7.5µm×7.5µm, (b) 10µm×10µm and 45 µm×45µm, (c) 1µm×45µm and 5µm×50µm, and (d) 1µm×93µm and 1µm×93µm.

5.2. Validation of the model for diagonal separation

Next, we validate the model by varying the diagonal separation between the contacts by simultaneously changing X_{ee} and Y_{cc} as shown in Figure 5.3. In Figure 5.4 the Z-parameters extracted from EPIC and the values predicted by the model have been compared. The Z_{12} model is found to be in good agreement with the EPIC values.
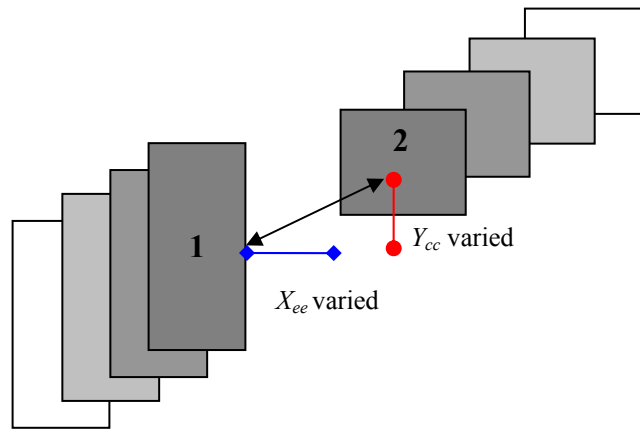
Figure 5.3. Contacts separated along the diagonal.
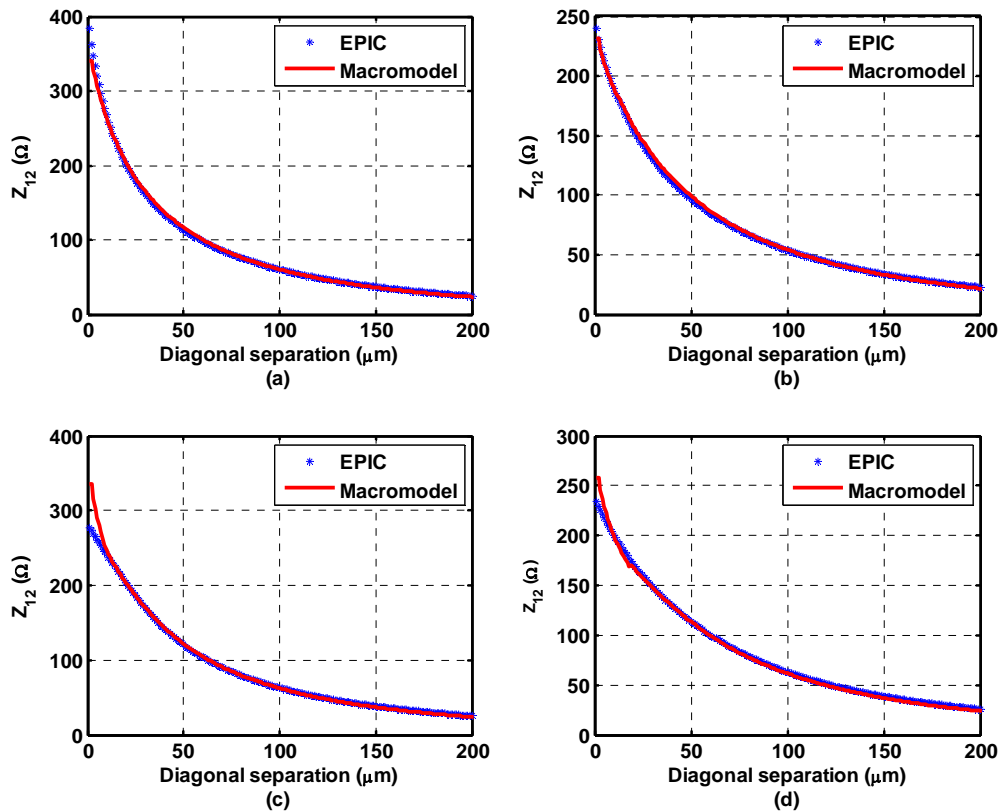
Figure 5.4. Comparison of model with EPIC simulations for diagonal separation with contact dimensions (a) 18μm×5μm and 2μm×15μm, (b) 30μm×30μm and 30μm x30μm, (c) 1μm x1μm and 5μm×73μm, and (d) 1μm x110μm and 5μm×100μm.

5.3. Validation using measurement results

The next set of validations for the macromodel, use resistance measurements for a TSMC 0.25μm lightly doped substrate. Figure 5.5 shows a cross section of the approximate doping profile for the substrate. While applying the process constants (obtained for the typical 0.25μm process) from Chapter 3, to model the self and mutual impedances for this substrate, the errors were observed to be as high as 40%.
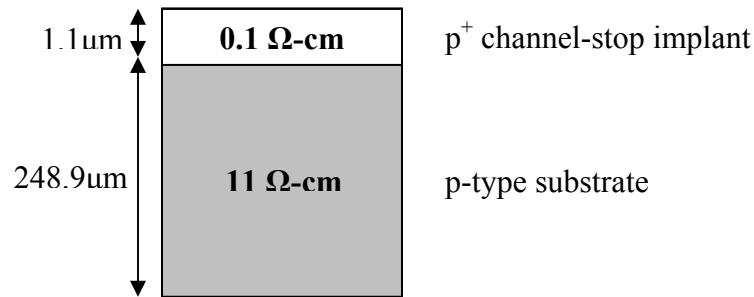
Figure 5.5. Layered doping profile for a lightly doped substrate.

Hence, measurements of 9 test structures (chosen randomly) were used for estimating the mutual-impedance process parameters and 2 were used for validating the model. The test structures have X_{ee} separations varying from 1μm to 100μm. So Equation (3.5) alone is used. The extracted process parameters for the mutual-impedance are:

k_1=2.22x10^{-14}Ω (μm)$^{-1}$ $\qquad$ k_2= 611.15Ω $\qquad$ k_3=0.158 (μm)$^{-0.5}$

The validation results are shown in Figure 5.6. The relative errors in cross-coupling impedances are about 15-20%. The errors are slightly higher than expected since the model parameters were extracted from a limited number of test structures.
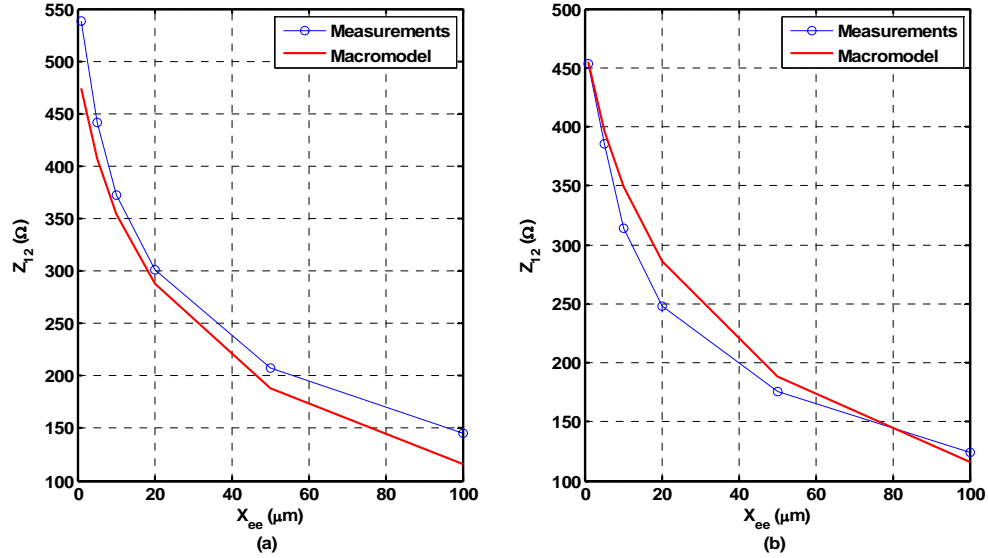
Figure 5.6. Comparison of the mutual impedance macromodel with measurement values for contact dimensions (a) 0.66μm×0.62μm and 0.66μm×1.18μm, and (b) 0.66μm×0.62μm and 0.66μm×11.98μm.

For the self-impedance model, all the test structures were used to extract the process constants. The results are shown in Figure 5.7. The errors relative to measurements are within ±6% and the process parameters were calculated as:

$\alpha_1 = 9.5\text{x}10^{-8}(\mu m)^{-2}\Omega^{-1}$ $\qquad\qquad$ $\alpha_2 = 3\text{x}10^{-6}(\mu m)^{-0.5}\Omega^{-1}$ $\qquad\qquad$ $\alpha_3 = 0.377$

$\alpha_4 = 5.56\text{x}10^{-5}\Omega^{-1}$
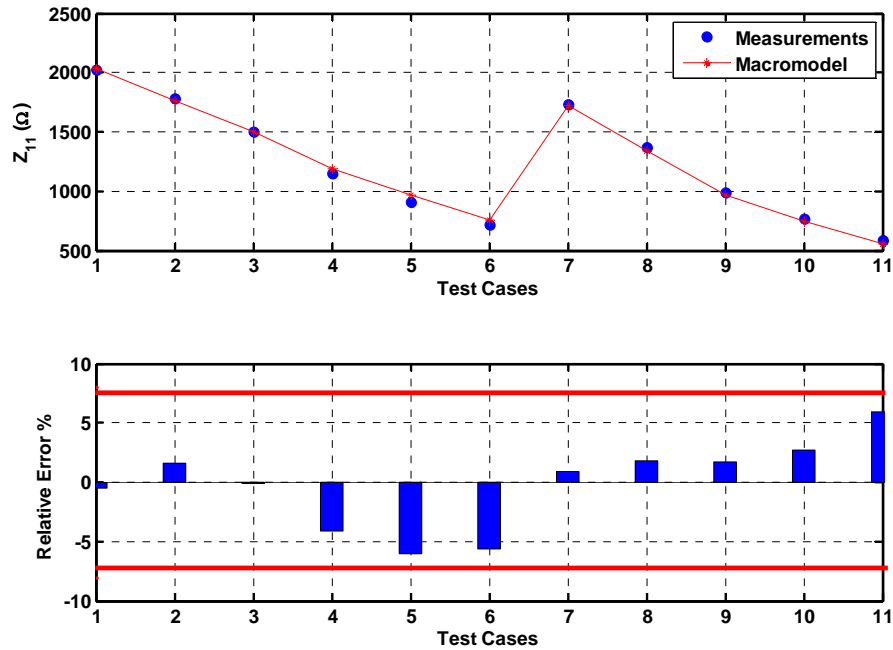
Figure 5.7. Validation of the self-impedance macromodel with measured values.
(a) Comparison of macromodel with measurements. (b) Errors relative to the
measurements.

5.4. Multi-contact Problem

The model has also been applied to a multi-contact example. A complex post
layout example of an RF LNA is used. An analysis of the substrate noise for the LNA has
been presented in [19]. A stepped buffer was used as the noise injector. The block
diagram for the stepped buffer and a circuit diagram for the LNA are provided in Figure
5.8. The operating frequency was set at 2.4GHz and hence the substrate network was
modeled as a resistive network. Figure 5.9 shows a simplified layout of the circuits. The
network consists of 51 contacts.

A simple model depicting the substrate network is shown in Figure 5.10. Noise is
injected into the substrate because of the switching activity of the inverters in the stepped

buffer. The injected noise propagates via the substrate and is picked up by the sensitive LNA.

EPIC was used to extract the equivalent substrate network in [18]. In this work, the macromodel in conjunction with the paneling approach is used to extract the equivalent substrate network.
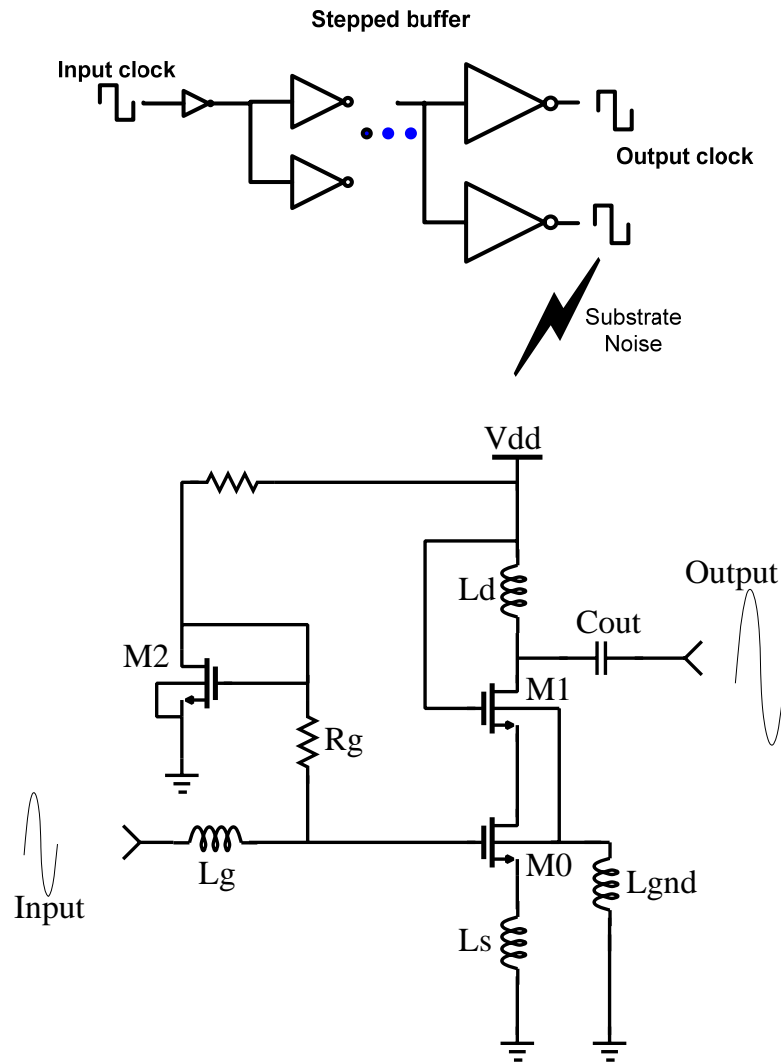
Figure 5.8. Block diagram for the stepped buffer and circuit schematic of the LNA.

This section evaluates the macromodel performance in terms of computation time and accuracy in comparison with EPIC for the circuit example. In Appendix F, a more complicated substrate network for the same circuit example (84 contacts) is considered for comparison of the macromodel with measurement results.
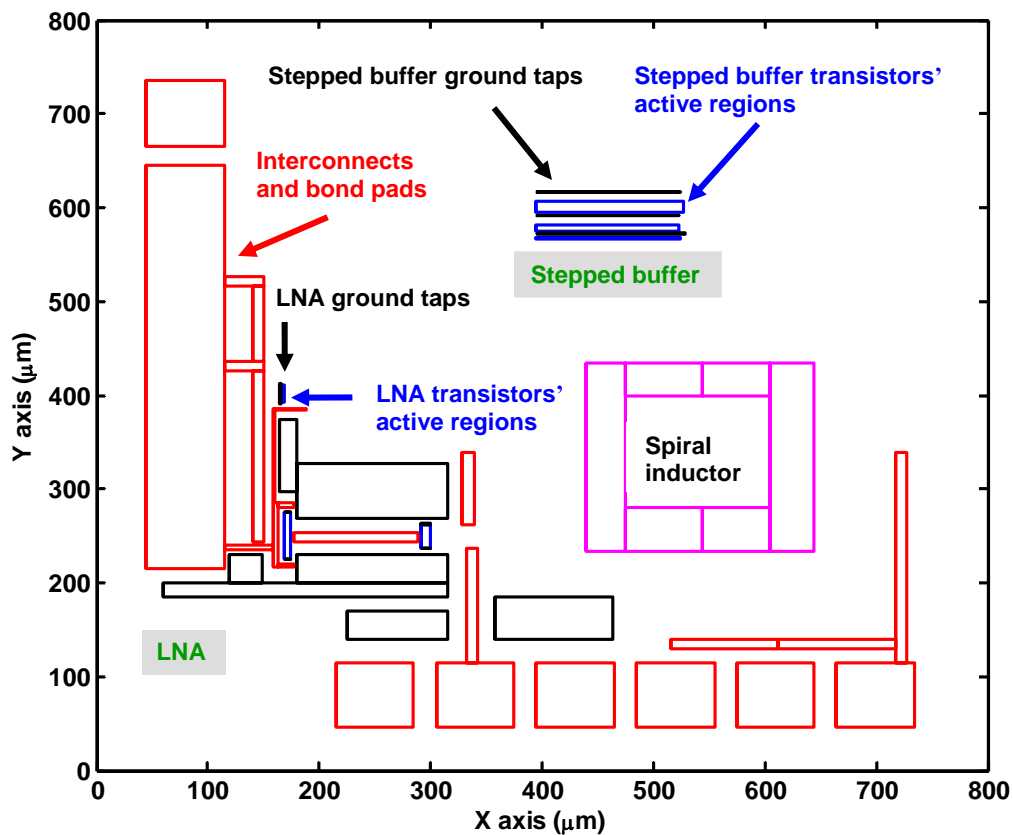
Figure 5.9. Layout of the LNA and stepped buffer with 51 contacts.
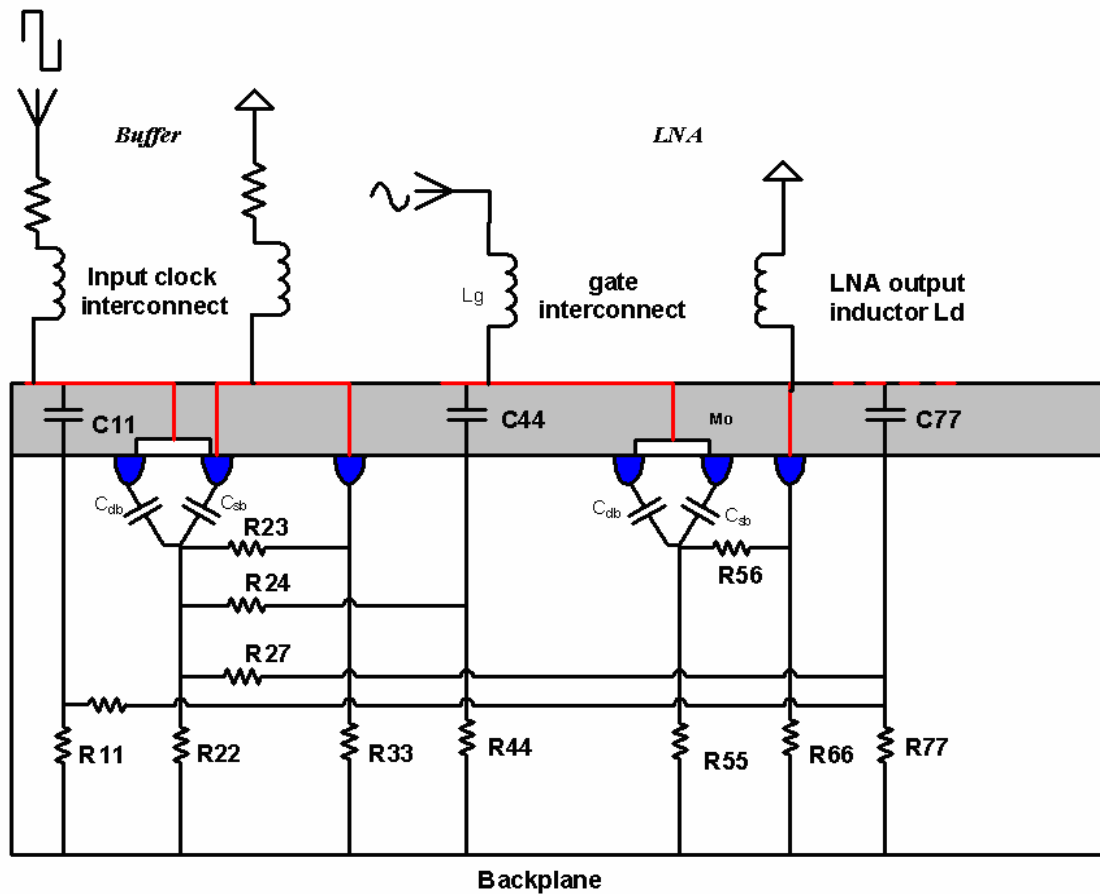
Figure 5.10. Cross section of the substrate network for LNA and stepped buffer in a lightly doped substrate.

The frequency spectrum of the LNA output is analyzed to evaluate the substrate noise. The important resistance values have been compared in Table 5.1. Though some of the errors are of the order of 20% they do not affect the output noise. The model applied with paneling is in good agreement with EPIC simulations as shown in Figure 5.10. The model applied without paneling does not predict the output noise spectrum as close as the model applied with paneling. The computation time for the model with paneling is only 9 minutes and 30 seconds, when compared to EPIC that took 5 hours and 38 minutes on a Redhat Linux (kernel version 2.6.9-34.EL) machine with 1GB RAM and a 3.2GHz CPU.

Table 5.1 Comparison of resistance values from EPIC and those generated from the macromodel.

Resistance values	EPIC (kΩ)	Macromodel (kΩ)	Error %
R_{ii} (LNA input transistor)	36.626	33.571	8.34%
R_{jj} (LNA output transistor)	35.08	39.43	-12.4%
R_{kk} (Buffer active region)	1.372	1.5482	12%
R_{k0} (Buffer active region to ground)	0.025	0.030	20%
R_{ll} (Buffer ground taps)	0.561	0.515	8.3%
R_{nn} (Interconnect)	0.349	0.339	2.8%
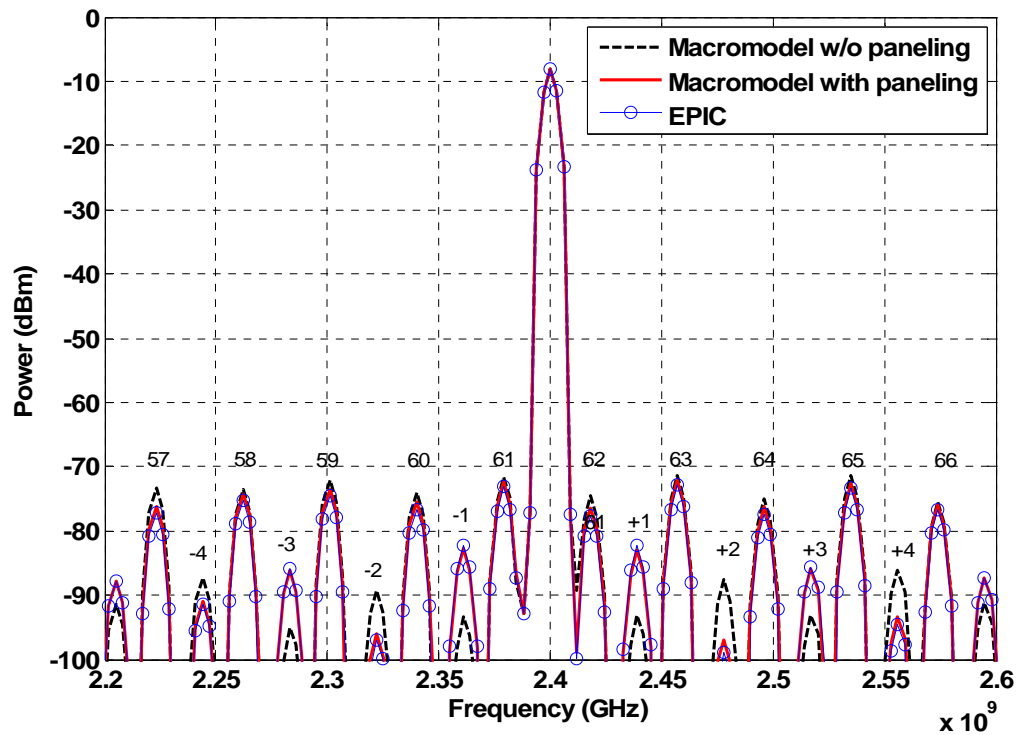
Figure 5.11. Comparison of spectrum of the LNA output using EPIC and the macromodel for the substrate network.

6. CONCLUSIONS

Substrate noise coupling is a critical issue when integrating analog, RF, and digital circuits on a common substrate. Lightly doped substrates are preferred for analog and RF applications as they provide better noise isolation. Efficient macromodels are needed for estimating the noise coupling in large systems-on-a-chip.

This work has presented a Z-parameter based macromodel that characterizes the lightly doped substrate as a resistive network. The model is scalable with contact geometry and separations. The two-contact model requires a total of nine process constants. The relative errors between the macromodel and EPIC simulation values are about 10-15% for a large set of contact dimensions and separations.

The cross-coupling impedance has been modeled using an improved geometric mean distance model. The modification alleviates the inaccuracies in the original GMD model for close separations. This is important as such cases are often encountered in practical layouts. The self-impedance model is enhanced with a paneling approach that accounts for the proximity of neighboring contacts. The paneling approach can also be used for resolving the GMD limitations in the mutual-impedance model at the expense of computation time. The entire model is in good agreement with simulation results.

The backplane of the lightly doped substrate has been approximated as a single node in this work. This assumption has been validated for thick substrates exceeding 200μm. The relationship between the die area and the substrate thickness for this assumption to be valid is not explored. This aspect needs to be examined further.

The thesis focuses on modeling the resistive substrate. With an increase in the frequency of operation, the substrate network becomes capacitive [20]. This frequency dependence needs to be modeled, for extending the application of the macromodel to higher operating frequencies.

BIBLIOGRAPHY

[1]   T. Blalack, J. Lau, F. J. R. Clement, and B. A. Wooley, "Experimental results and modeling of noise coupling in a lightly doped substrate," *International Electron Devices Meeting*, pp. 623-626, December 1996.

[2]   T. Blalack, Y. Leclercq, and C. P. Yue, "On-chip RF isolation techniques," *IEEE Proc. of Bipolar/BiCMOS Circuits and Technology Meeting*, pp. 205-211, October 2002.

[3]   B. R. Stanisic, N. K. Verghese, R. A. Rutenbar, L. R. Carley, and D. J. Allstot, "Addressing substrate coupling in mixed-mode ICs: simulations and power distribution synthesis," *IEEE Journal of Solid State Circuits*, vol. 29, pp. 226-238, March 1994.

[4]   I. L. Wemple and A. T. Yang, "Integrated circuit substrate coupling models based on Voronoi-Tessellation substrate macromodels," *IEEE Transactions on Computer-Aided Design*, pp. 1459-1469, December 1995.

[5]   C. G. Xu, "EPIC: A program for extraction of substrate resistance with the Green's Function method," Department of ECE, Oregon State University, 2003.

[6]   R. Gharpurey and R. G. Meyer, "Modeling and analysis of substrate coupling in integrated circuits," *IEEE Journal of Solid State Circuits*, vol. 31, pp. 344-352, March 1996.

[7]   M. Koteeswaran, "Substrate coupling macromodel for lightly doped CMOS processes," *M.S. Thesis*, Oregon State University, July 2003.

[8]   H. Lan, T. W. Chen, C. O. Chui, and R. W. Dutton, "Compact modeling and experimental verification of substrate resistance in lightly doped substrates," *SASIMI 2004*, pp. 189-195, October 2004.

[9]   H. Lan and R. W. Dutton, "Synthesized compact models (SCM) of substrate noise coupling," *Unpublished Report*, Dept. of Electrical Engineering, Stanford University, CA, Nov. 2002.

[10]   X. Aragones, J. L. Gonzalez, and A. Rubio, Ed. *Analysis and Solutions for Switching Noise Coupling in Mixed-Signal ICs* Boston, MA: Kluwer, 1999.

[11]   D. Ozis, T. Fiez, and K. Mayaram, "An efficient modeling approach for substrate noise coupling analysis," *IEEE International Symposium on Circuits and Systems*, vol. 5, pp. 237-240, May 2002.

[12] H. Lan, T. W. Chen, C. O. Chui, P. Nikaeen, J. W. Kim, R. W. Dutton, "Synthesized compact models and experimental verifications for substrate noise coupling in mixed-signal ICs," *IEEE Journal of Solid-State Circuits*, vol. 41, no. 8, pp. 1817-1829, August 2006.

[13] MEDICI - Two dimensional process simulation program, Version 2000.2.1, Avant! Corporation, 2000.

[14] T. J. Higgins, "Theory and Application of Complex Logarithms and Geometric Mean Distances", *Trans. AIEE*, vol. 66, pp. 12-16, 1947.

[15] S. K. Arunachalam, "An efficient and accurate method of estimating substrate noise coupling in heavily doped substrates," *M.S. Thesis*, Oregon State University, August 2005.

[16] C. G. Xu, T. Fiez, and K. Mayaram, "An improved Z-parameter macro model for substrate noise coupling," *IEEE International Symposium on Circuits and Systems*, pp. 23-26, May 2004.

[17] A. Sharma, "Predictive methodologies for substrate parasitic extraction and modeling in heavily doped substrates CMOS substrates," *M.S. Thesis*, Oregon State University, July 2003.

[18] N. K. Verghese, "Extraction and simulation techniques for substrate coupled noise in mixed signal integrated circuits," *Ph.D. Dissertation*, Carnegie Mellon University, August 1995.

[19] S. Hazenboom, "A comparison of substrate noise coupling in lightly and heavily doped CMOS processes for 2.4GHz LNAs," *M.S. Thesis*, Oregon State University, June 2004.

[20] C. G. Xu, T. Fiez, and K. Mayaram, "High frequency lumped element models for substrate noise coupling," *Proceedings of the International Workshop on Behavioral Modeling and Simulation*, pp. 47-50, October 2003.

APPENDICES

APPENDIX A

EPIC (Extraction of Parasitics in Integrated Circuits) is a Green's function-based solver. The tool characterizes the silicon substrate using a multilayered structure. The resistivity and thickness of each of these layers is obtained from the substrate doping profile. Solving the Green's function yields the potential at a point on the substrate due to an electric charge at another point. For more information on the solver options, refer to [5].

The version of the tool used for this work characterizes the substrate as a resistive network assuming low frequency operation. Also, the tool assumes contacts on the substrate to be 2-D, i.e., there is no depth specification required for describing the contacts. In addition, adjacent contacts are not automatically considered physically merged. The input data has to specify adjacent contacts to be equipotential.

The discrete cosine transforms (DCT) are used by EPIC to perform a fast computation of the Z-matrix. By default, the backplane of a substrate is grounded by adding a low resistive layer to the substrate's backside. To keep the backplane floating, the input file has to be modified by adding a high resistive layer to the backside of the substrate.

APPENDIX B

To show that the backplane of a lightly doped silicon substrate can be considered an equipotential surface when the substrate thickness is large, a multi-contact example is considered. The contacts have large dimensions and are placed in a 1mm×1mm die. The layout is shown in Figure B-1. Table B-1 compares some of the *effective coupling resistance* values with worst case errors when the backplane is assumed equipotential for a substrate thickness of 250 μm.
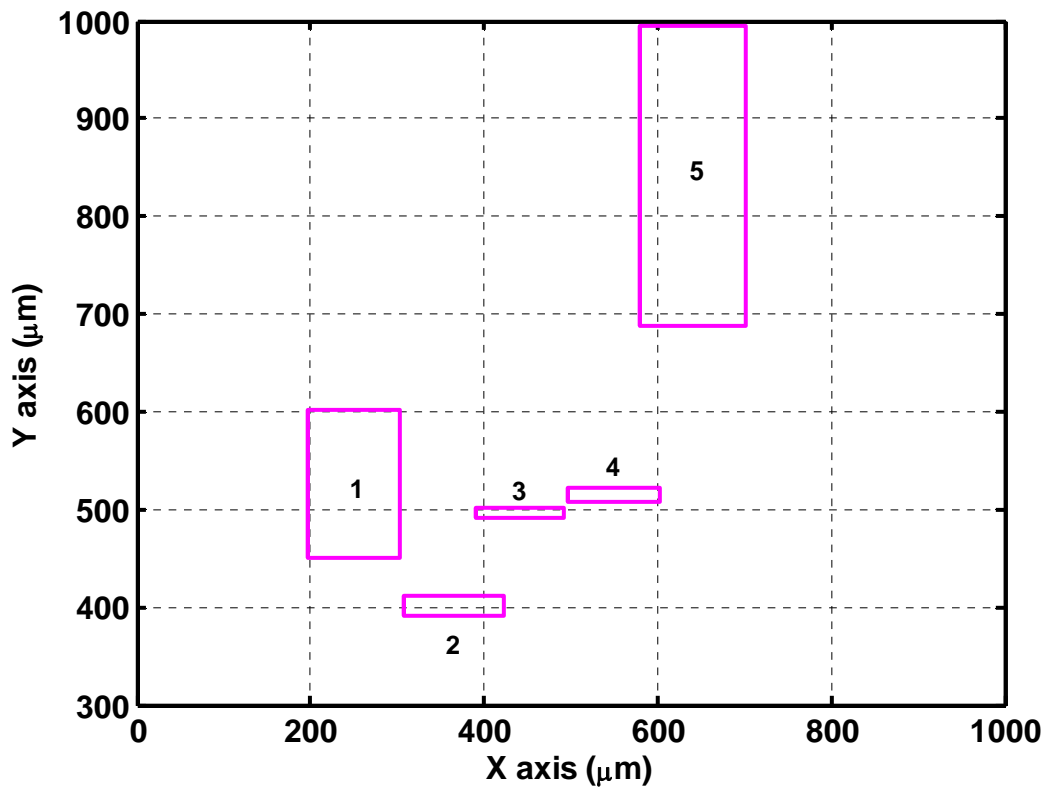
Figure B-1 Layout of five big contacts in a 1mm×1mm die.

Table B-1. Comparison of *effective cross-coupling resistances* from a floating backplane setup and those derived from a grounded backplane for a multi-contact system in a 250μm thick substrate.

R_{ij}	From floating backplane(Ω)	Extracted from grounded backplane(Ω)	Relative Error
R_{12}	212.65	206	3%
R_{14}	290.45	271.6	6.4%
R_{25}	334	280	16%
R_{45}	283.35	260.09	8%

The above multi-contact example is now tested using a resistive ground connection. Instead of directly grounding the substrate backplane, a resistive layer is added to simulate an improper ground connection (Figure B-2).
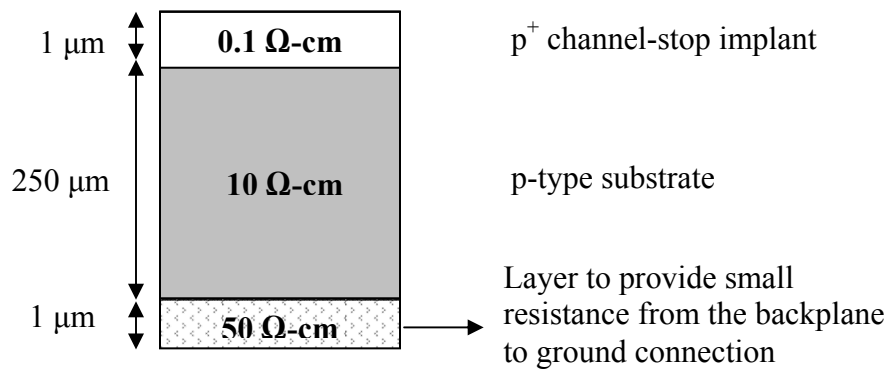
Figure B-2. Cross section of the doping profile for a typical 0.25μm process lightly doped substrate with a resistive ground connection.

It was observed that the equipotential backplane assumption holds good even with a resistive ground connection. In fact there were no changes in the effective cross-

coupling resistance values derived from the two situations: grounding the substrate backplane directly and grounding the substrate backplane through a small resistance.

For a substrate thickness of 100μm, the multi-contact example is used for testing the equipotential backplane assumption. The maximum errors due to this assumption are of the order of 40%.

Table B-2. Comparison of the *effective cross-coupling resistances* from a floating backplane setup and those derived from a grounded backplane for a multi-contact example in a 100μm thick substrate.

R_{ij}	From floating backplane(Ω)	Extracted from grounded backplane(Ω)	Relative Error
R_{12}	225	195	13%
R_{14}	333.33	250	25%
R_{25}	409.83	230	43%
R_{45}	322.8	230	28%

As the bulk thickness reduces below 200μm, the backplane equipotential assumption becomes invalid. For processes considered in this work, the single node approximation of the backplane is valid as the substrate thickness was 250μm.

APPENDIX C

The choice of the geometric data set is very important as mentioned in Chapter 3.2. The following figure represents the types of contacts and orientation included in the data set.
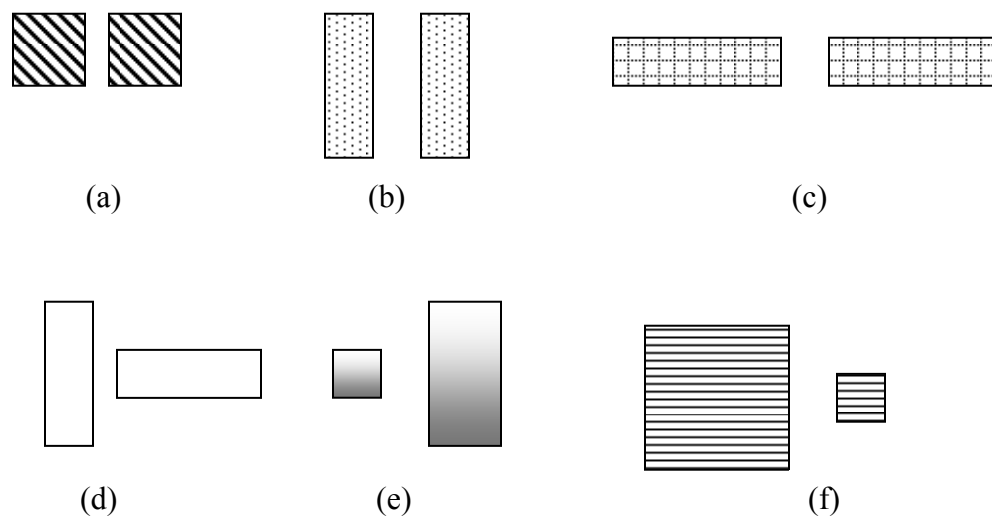
Figure C-1. Geometric cases and orientations considered for the model development. (a) Identical square contacts. (b) Identical rectangular contacts with large lengths. (c) Identical rectangular contacts with large widths. (d) Identical rectangles oriented differently. (e), (f) Non identical contacts.

The geometric test cases included for the macromodel development are listed in Table C-1.

Table C-1. Geometric cases for the model development.

Test case #	W1	L1	W2	L2
1.	1.2	1.2	1.2	1.2
2.	2	2	2	2
3.	3	3	3	3
4.	4	4	4	4
5.	5	5	5	5
6.	6	6	6	6
7.	8	8	8	8

8.	10	10	10	10
9.	12	12	12	12
10.	14	14	14	14
11.	16	16	16	16
12.	18	18	18	18
13.	20	20	20	20
14.	20	20	5	5
15.	20	5	5	5
16.	20	5	20	5
17.	20	5	5	20
18.	2	2	5	5
19.	2	5	5	2
20.	2	2	3	3
21.	4	3.6	2.8	3.2
22.	2.5	3	4	2
23.	6	8	9	5
24.	10	16	3	3
25.	25	7	16	20
26.	18	14	3.6	2.5
27.	3	1	2	2.4
28.	4	3.6	2.8	1.2
29.	4	2	4	2
30.	1	2	2	2
31.	2	5	3	3
32.	3	5	2	4.5
33.	10	10	5	4
34.	15	12	8	20
35.	20	2	5	8
36.	20	10	20	10
37.	6	3	6	3
38.	10	5	10	5
39.	2.4	1.2	2.4	1.2
40.	16	18	25	18
41.	5	19	4	16
42.	6	9	8	12
43.	20	2	20	2
44.	20	4	20	4
45.	20	3	20	3
46.	18	10	2	10
47.	15	10	5	10
48.	10	18	10	2
49.	10	15	10	5
50.	18	15	2	5
51.	18	5	2	15
52.	18	18	2	2
53.	18	2	2	18
54.	15	18	5	2
55.	15	2	5	18
56.	15	15	5	5
57.	15	5	5	15
58.	20	2	2	2

59.	2	20	2	2
60.	10	3	3	16
61.	25	20	16	7
62.	18	2.5	3.6	14
63.	3	2.4	2	1
64.	4	1.2	2.8	3.6
65.	4	2	4	2
66.	2	2	1	2
67.	3	5	2	3
68.	2	5	3	4.5
69.	5	10	10	4
70.	1	30	2	2
71.	25	25	25	25
72.	30	30	30	30
73.	40	40	40	40
74.	50	50	50	50
75.	70	70	70	70
76.	90	90	90	90
77.	100	100	100	100
78.	125	125	125	125
79.	150	150	150	150
80.	200	200	200	200
81.	1	30	1	30
82.	1	40	1	40
83.	1	100	1	100
84.	5	40	5	40
85.	10	40	10	40
86.	20	40	20	40
87.	5	80	4	90
88.	3	80	4	100
89.	10	75	5	150
90.	6	180	5	150
91.	24	6	6	90
92.	30	6	6	90
93.	50	3	50	5
94.	60	2	45	1
95.	125	1	125	5
96.	1	200	1	1
97.	.5	200	15	2
98.	.5	100	15	15
99.	.5	200	15	15
100.	1	110	5	73
101.	1	110	5	20
102.	1	110	5	27
103.	1	110	5	108
104.	1	110	5	1
105.	1	110	1	1
106.	5	20	5	73
107.	1	1	5	73
108.	1	1	5	108
109.	5	20	5	108

110.	1	110	5	10
111.	1	110	5	50
112.	1	110	5	100
113.	1	110	10	5
114.	1	110	50	5
115.	1	110	100	5

APPENDIX D

The process parameters for the model are extracted by a least-squares curve fitting procedure. The built-in function of MATLAB is used. This section will explain the procedure for extracting the process parameters for the GMD model. A similar procedure is followed for obtaining the parameters for the rest of the model.

The objective function for the curve fitting procedure is:

$$\min \sum_1^m \left| \frac{Z_{mod} - Z_{sim}}{Z_{sim}} \right|^2$$

where m is the number of data points, Z_{mod} is the model generated Z values given by say $Z_{mod} = [k_1(w_1 + w_2) + k_2]e^{-k_3\sqrt{gmd}}$ and Z_{sim} is the EPIC generated Z values. The process constants for the model are extracted from:

$$k = \arg\min\left(\sum_1^m \left| \frac{Z_{mod} - Z_{sim}}{Z_{sim}} \right|^2 \right)$$

where k is the vector containing the process constants for the model equation and arg min returns the vector k that minimizes the sum of squares of the relative errors. The normalized Z values are used for the curve-fitting process instead of the simple difference, to make the procedure more robust.

APPENDIX E

The model development procedure used 115 contact geometries. However, to extract the process constants of the macromodel for other processes, such a large data set may not be available and hence the data set requirements need to be explored.

From the available data set, a large number of contact geometries with small dimensions ($<20\mu m$) representing different orientations are excluded to create a new data set with 64 test cases. The excluded data set contains contact geometries from Test case #14 to #64 from Table C-1 (shaded). The process parameters for the model equations for the new data set are extracted using the least-squares curve fitting procedure. The comparison between the old process constants and the new process constants are shown in Table E-1.

Table E-1. Comparison of process constants extracted using 115 test cases and 64 test cases.

Process constant	Value with 115 Test Cases	Value with 64 Test Cases
k_1	0.2322	0.2384
k_2	638	637.34
k_3	0.195	0.195
k_4	0.002	0.002
k_5	0.25	0.25
α_1	9.5×10^{-8}	9.5×10^{-8}
α_2	3×10^{-6}	3.2×10^{-6}
α_3	0.5	0.5
α_4	4.6×10^{-4}	4.27×10^{-4}

It can be observed that the process constants do not undergo significant changes as a result of using the new data set. Also, the model equations with the new process constants, were validated for the excluded data set and resulted in similar error performance with the original model equations. Hence, the new data set can be considered as an optimized data set. The contact geometries are listed in Table E-2.

Table E-2. Geometric test cases for the optimized data set.

Test Cases #	W1	L1	W2	L2
1.	1.2	1.2	1.2	1.2
2.	2	2	2	2
3.	3	3	3	3
4.	4	4	4	4
5.	5	5	5	5
6.	6	6	6	6
7.	8	8	8	8
8.	10	10	10	10
9.	12	12	12	12
10.	14	14	14	14
11.	16	16	16	16
12.	18	18	18	18
13.	20	20	20	20
14.	4	2	4	2
15.	2	2	1	2
16.	3	5	2	3
17.	2	5	3	4.5
18.	5	10	10	4
19.	1	30	2	2
20.	25	25	25	25
21.	30	30	30	30
22.	40	40	40	40
23.	50	50	50	50
24.	70	70	70	70
25.	90	90	90	90
26.	100	100	100	100
27.	125	125	125	125
28.	150	150	150	150
29.	200	200	200	200
30.	1	30	1	30
31.	1	40	1	40
32.	1	100	1	100
33.	5	40	5	40
34.	10	40	10	40

35.	20	40	20	40
36.	5	80	4	90
37.	3	80	4	100
38.	10	75	5	150
39.	6	180	5	150
40.	24	6	6	90
41.	30	6	6	90
42.	50	3	50	5
43.	60	2	45	1
44.	125	1	125	5
45.	1	200	1	1
46.	.5	200	15	2
47.	.5	100	15	15
48.	.5	200	15	15
49.	1	110	5	73
50.	1	110	5	20
51.	1	110	5	27
52.	1	110	5	108
53.	1	110	5	1
54.	1	110	1	1
55.	5	20	5	73
56.	1	1	5	73
57.	1	1	5	108
58.	5	20	5	108
59.	1	110	5	10
60.	1	110	5	50
61.	1	110	5	100
62.	1	110	10	5
63.	1	110	50	5
64.	1	110	100	5

APPENDIX F

In order to compare the performance of the macromodel with measurement results the entire substrate network consisting of 59 contacts is considered. The layout of the contact geometries is shown in Figure F-1. Compared to the layout presented in Section 5.4, this layout includes more contacts.
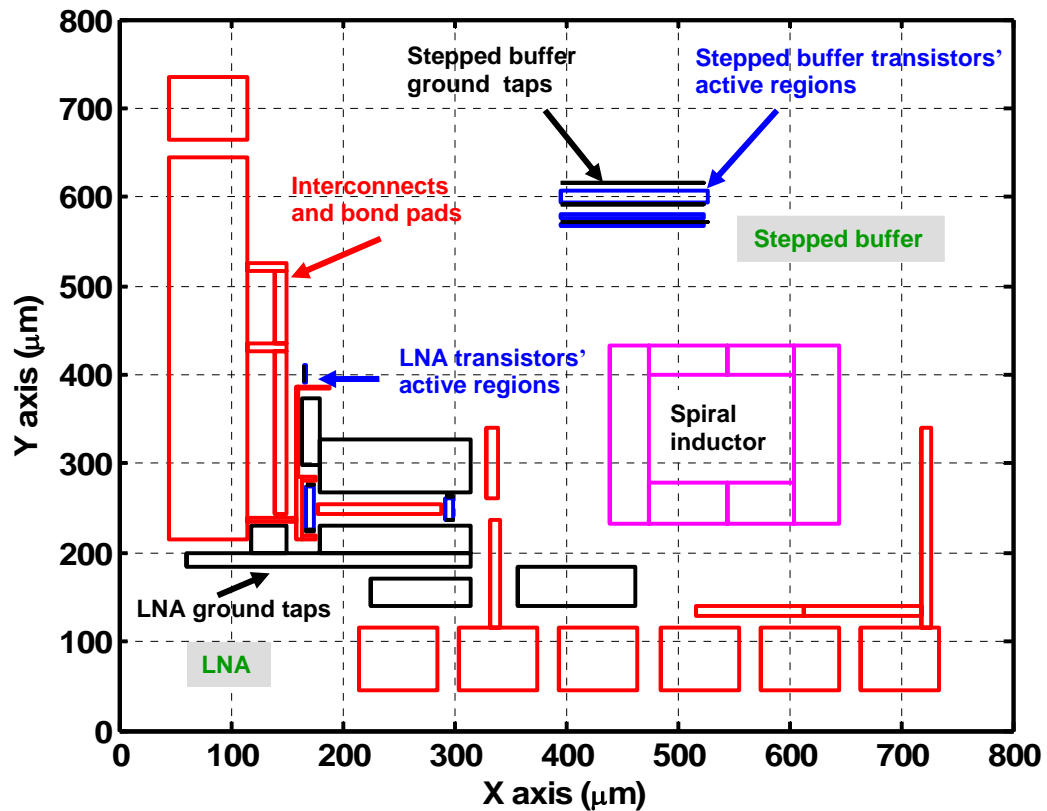

Figure F-1. Layout of contacts for an LNA and stepped buffer circuit with 59 contacts.

The model parameter extraction is carried out using the optimized data set and the substrate profile shown in Figure 5.5 from EPIC simulations. The substrate network is

obtained by applying the paneling approach to the macromodel. The frequency spectrum

of the LNA output is analyzed to estimate the substrate noise. The model is reasonably

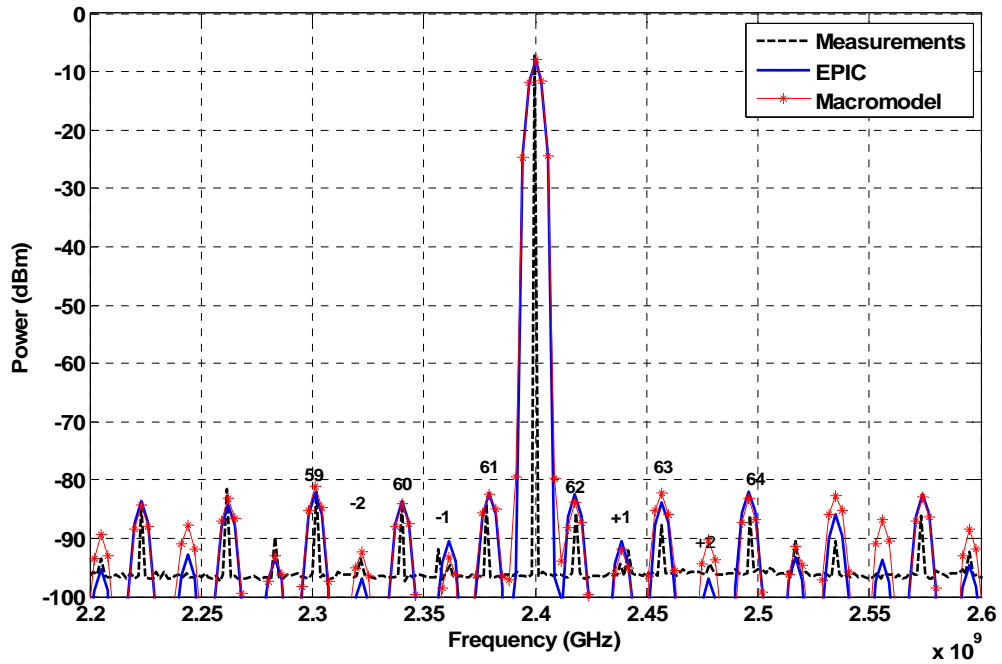accurate when compared to EPIC and measurement results as shown in Figure F-2.

Figure F-2. Comparison of LNA output spectrum using macromodel, EPIC and
measurements.